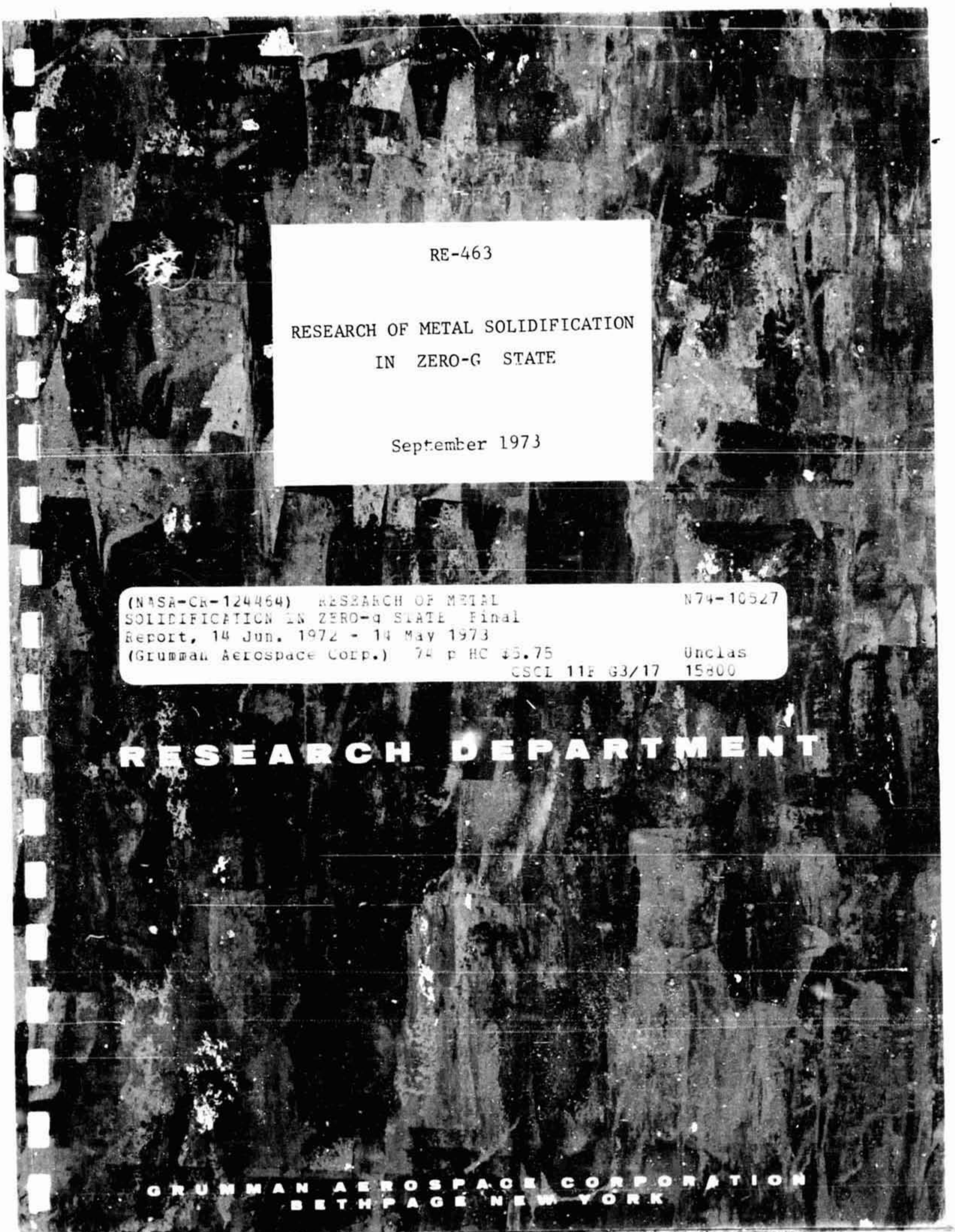

RE-463

RESEARCH OF METAL SOLIDIFICATION IN ZERO-G STATE

September 1973

(NASA-CR-124464) RESEARCH OF METAL SOLIDIFICATION IN ZERO-g STATE Final Report, 14 Jun. 1972 - 14 May 1973 (Grumman Aerospace Corp.) 74 p HC $5.75 CSCL 11F G3/17

N74-10527

Unclas 15800

RESEARCH DEPARTMENT

GRUMMAN AEROSPACE CORPORATION
BETHPAGE NEW YORK

RESEARCH OF METAL SOLIDIFICATION
IN ZERO-G STATE

FINAL REPORT

(Reporting Period: June 14, 1972 to May 14, 1973)

RE-463

William M. Aubin

Dave Larson, Jr.

Gary I. Geschwind

Research Department
Grumman Aerospace Corporation
Bethpage New York 11714

Prepared under Contract NAS 8-28604

for the

National Aeronautics and Space Administration
George C. Marshall Space Flight Center
Marshall Space Flight Center, Alabama 35812

September 1973

Approved by:
Charles E. Mack, Jr.
Director of Research

ABSTRACT

An experiment test apparatus that allows metal melting and resolidification in the three seconds available during free fall in the Marshall Space Flight Center drop tower was built and tested in the tower. Droplets (∿ 0.05 cm) of pure nickel and 1090 steel were prepared in this fashion. The apparatus, including instrumentation, is described. As part of the instrumentation, a method for measuring temperature-time histories of the free floating metal droplets was developed. Finally, there is presented a metallurgical analysis of the specimens prepared in the apparatus.

ACKNOWLEDGMENTS

The program described in this report is the work of many people. Leroy H. Berge, the contracting officer's representative, was always ready with suggestions or encouragement when needed. The MSFC drop tower team performed with dedication, and our interface with the team was smoothed by the constant attention of V. Yost and L. Ramsey, the P.E. Laboratory personnel responsible for the drop tower experiments.

At Grumman, the design team of E. Kennelly, M. Kesselman, and V. Taibbi handled the entire design and fabrication. Laboratory technicians C. Lottermoser and W. Poit worked both at Grumman and at MSFC in conducting experiments. All of the thermal diagnostics was carried out by G. Busch and T. Hilgeman. Finally, A. Cobrin and M. Sudwischer carried out the editing and typing of this report.

The authors wish to thank everyone for their help and assistance. The team effort has made our job much easier.

TABLE OF CONTENTS

LIST OF ILLUSTRATIONS

Figure		Page

INTRODUCTION

The exploitation of the space environment for materials processing is very attractive. This environment, unobtainable in an earthbound laboratory, could allow the development of new materials with vastly improved properties. How we bring about the full utilization of this environment to carry out unique types of materials processing, however, is both subtle and perplexing. This is true because the zero gravity of space, the feature most likely to affect materials processing, is quite difficult to realize short of orbital flight. Also, most scientists and engineers have spent only a few years contemplating the full meaning of this new environment.

In the present program, conducted under partial support from NASA under Contract NAS 8-28604, Grumman Aerospace Corporation has explored the use of a free fall facility, located at NASA/Marshall Space Flight Center, to study the effects of zero gravity on metal melting and solidification. The facility is described in detail in Ref. 1. In essence, one is able to obtain a full three seconds of zero gravity test time. For this brief time, the environment is very close to an absolute zero gravity.

The effects of zero gravity on metal melting and solidification can best be understood if we have a facility in a zero gravity environment that is capable of producing solidified specimens in the absence of a crucible with controlled specimen heating and cooling rates, controlled degree of superheat and undercooling, specimen centering or drift control, and controlled atmosphere, while recording the free floating specimen temperature-time history. The facility should also be able to handle specimens of a sufficient size that both microstructure and mechanical properties can be determined.

In the present contract, we have taken a first step toward this ultimate facility. The experiment test package developed under the contract has indirect (and limited) control over heating and cooling rates, no control over superheat or undercooling, no drift control (but, because of low initial forces and uniform specimen heating, very low specimen drift rates), a potential for high vacuum, and, finally, the capability of monitoring the temperature-time history. Specimen size is too small at present for measurement of properties; it is, however, adequate for microstructure determination.

This report describes the design and fabrication of the test apparatus outlined above and discusses the preliminary tests conducted both in the laboratory and in the Marshall drop tower. Microstructural analysis of the specimens prepared both in the laboratory and during free fall in the test package was carried out, and these results are presented.

PROGRAM AIMS

The task of ascertaining the effect of zero gravity on metal melting and solidification is simplified if some time is spent on predicting results. If certain results are anticipated, they are far easier to detect than effects that were not expected. For this reason, an extensive effort was expended in attempting to state in advance of experimentation what the effect of zero gravity metal processing would be.

Under separate contract (NAS 8-27891), we developed analytical tools to study segregation effects in zero gravity. This work (Ref. 2) showed that metal droplets solidifying under zero gravity (freely suspended in space) would solidify from the surface toward the center and that the microstructure of the droplets would be strongly dependent upon cooling rate. The analysis showed that for very slow cooling the surface structure would be equiaxed hexagonal grains that would proceed to grow toward the sphere center. The final microstructure would display complete spherical symmetry and a hollow core due to material shrinkage upon cooling.

Our analytical work gave us other information. A model of surface evaporation of binary alloys (Ref. 3) showed the importance of evaporative segregation. Of more significance for a free floating molten specimen was the equivalent "g" field brought about by differential evaporation due to differential heating. Any heat gradient will result in an acceleration of the specimen due to jetting action.

Finally, consideration of the spatial environment and consultation with personnel having considerable undercooling experience led us to the conclusion that metals cooled in zero gravity should be experiencing a considerable degree of undercooling. There is no thermal convection, no container, and a very low vibration environment. All of these factors will decrease the probability of nucleation and growth of the solid phase.

The amount of undercooling can be determined by examination of the specimen microstructure after solidification in zero gravity. The undercooled specimen has a spherical grain structure that becomes more equiaxed, finer, and more spherical as the degree of undercooling increases (Ref. 4).

Undercooling takes on a special importance in this program because we do not see that the zero gravity environment will have a direct effect on the microstructure of polycrystalline materials. Undercooling, however, has a marked effect on microstructure. Furthermore, preliminary studies (Refs. 4 and 5) show that mechanical properties are continually improved as the undercooling increases. Here then is a way of realizing significant improvements in the mechanical properties of polycrystalline materials.

This section is intended to point the direction for the experimental analysis described in the following sections. It should be made clear at this time, however, that this program is a continuing one. The limitations in both time and funds dictated that the first part of the program (covered by this report) be intended primarily to confirm the experimental approach. The present effort culminated with two series of drops in the MSFC drop tower. These drops confirmed the effectiveness of the experimental approach, pointed out several shortcomings of the hardware as it is presently constituted, and supplied us with both high carbon steel and pure nickel specimens that had been melted and solidified in the three-second free fall time of the drop tower. These specimens have been examined microstructurally and results compared with specimens prepared in the laboratory.

HARDWARE DESIGN AND DEVELOPMENT

In the present contract, we are required to design and develop an experiment package that will melt and solidify metals in vacuum and in zero g. The package is to be capable of: 1) being tested in the drop tower at Marshall Space Flight Center and (2) being launched into a zero g trajectory by an Aerobee rocket.

The Aerobee rocket places a maximum size limit on the package of 15 inches diameter and 36 inches long. The drop tower imposes a deceleration load of 25 g's on the package and has a zero g profile of approximately 3 seconds.

Because of the short time duration of zero g in the drop tower, specimens were direct resistance melted. In this melting method, an unstable liquid column is first formed that changes its shape through surface tension forces to one of lower [illegible]y. Thus, the column first forms a series of unduloids that ultimately separate into a series of spheres (Ref. 6). Figure 1 shows this sequence.

For simplicity of fabrication, a cylindrical vacuum chamber ① was designed. (All circled numbers refer to parts shown in Fig. 2.) The cover ㉑ on one end is secured by a quick acting clamp ㉒. The cover contains two high current feed-throughs ⑯ on which are fastened two adjustable buss bars ⑤, which accommodate various length samples ⑫. The buss bars are braced so as to take the deceleration loads. The cover also has a viewing port ③, an eight-pin low voltage feed-through ⑮, and a mirror and positioning arm (④ and ⑩). On the other end of the chamber, there is a viewing port for the NASA-supplied high speed motion picture camera ⑨, a vacuum valve ⑭, and a vacuum gauge ⑰. For the drop tower experiment, the chamber and camera are fastened to a NASA-supplied 36 inch x 36 inch x 18 inch instrument package frame.

Fig. 1 Tungsten Wire Being Resistance Melted in the Laboratory

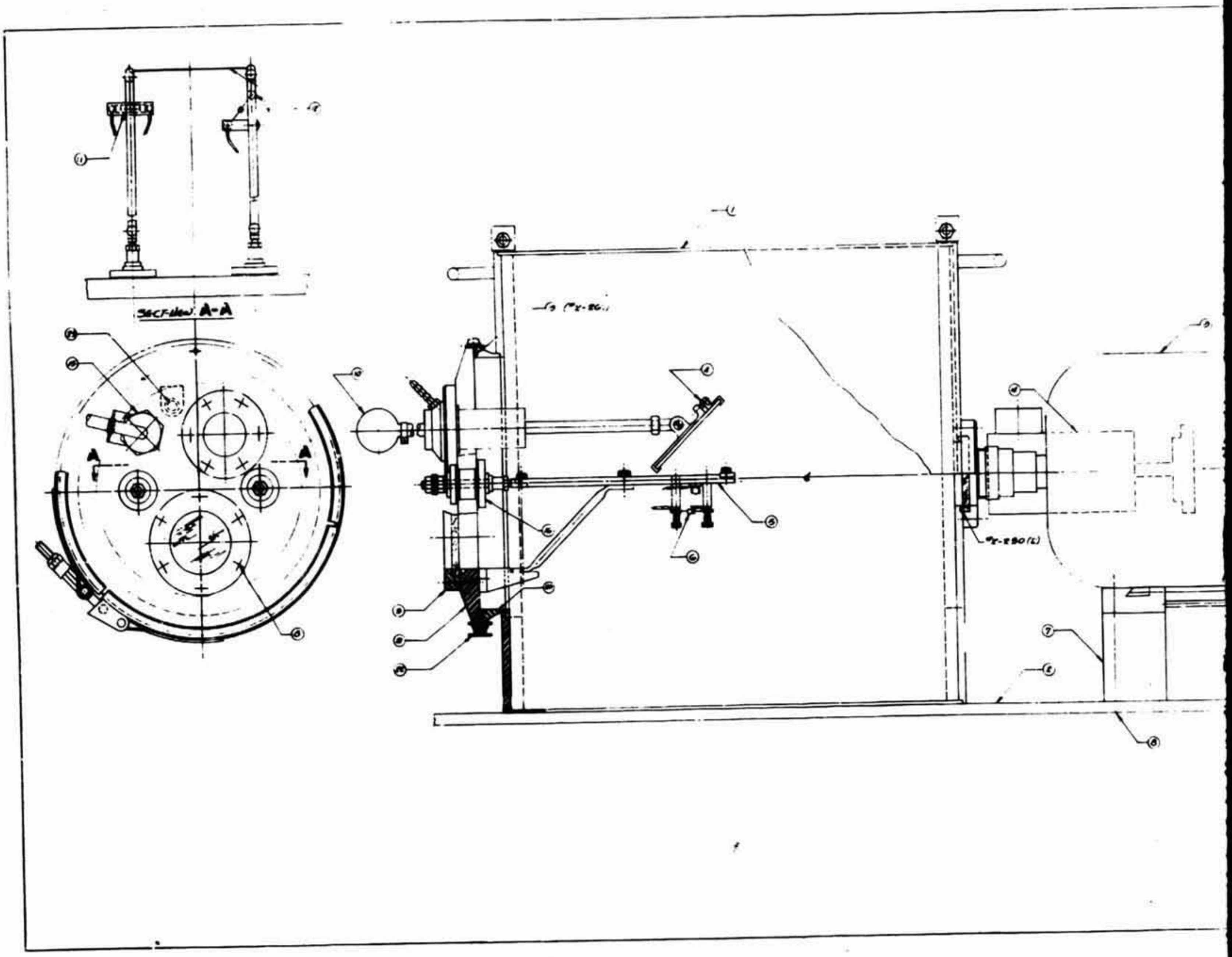
SECT-VIEW A-A
A
A

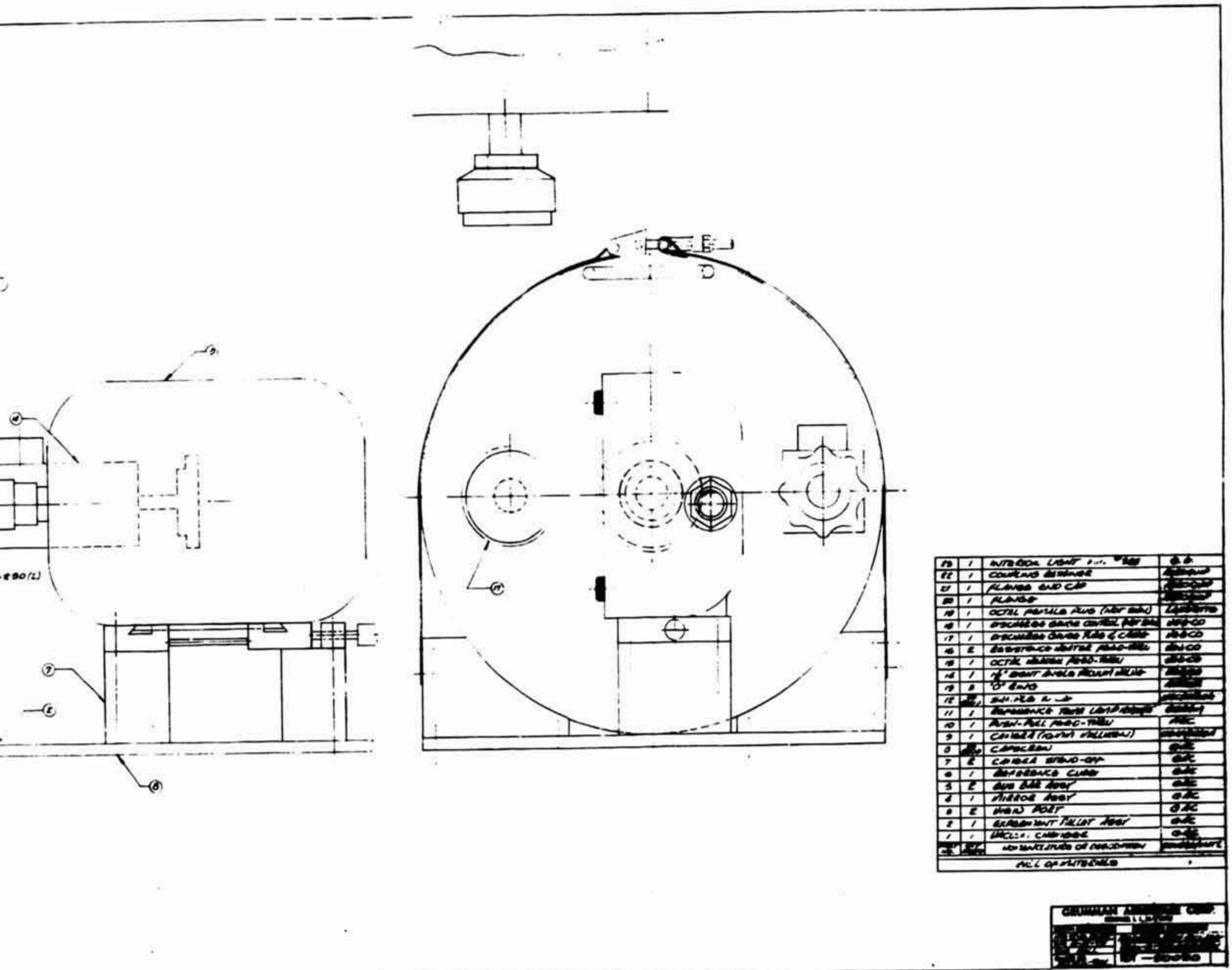

Fig. 2 Drawing of Chamber

FOLDOUT FRAME 2

Mounted on one of the buss bars that pass through the cover and within view of the camera, there is a reference filament ⑪ for measuring sample temperature. On the other buss bar, there is mounted a reference cube ⑥. This mass is released at the beginning of the drop by quickly melting a fine wire on which it is suspended. Its position with respect to time is recorded by the camera. This is done to verify that the samples are not accelerating due to some internal forces. The reference cube, however, was never illuminated sufficiently to be seen by the camera during the two series of drops.

The electronic system consists of four major packages (see Fig. 3):

- NASA-supplied battery pack to power the specimen
- NASA-supplied timing relays and control panel
- Specimen vacuum system and experiment wiring
- Telemetry amplifier and signal conditioner

Battery Pack

The battery pack is made up of nickel cadmium rechargeable cells packaged in two containers and wired in series, resulting in two 14.5 volt batteries wired in series. The containers are easily separated, providing essentially two independent 14.5 volt batteries.

Control Panel

The control panel (Fig. 3) has been programmed to control all aspects of the experiment. Upon receipt of the drop sequence

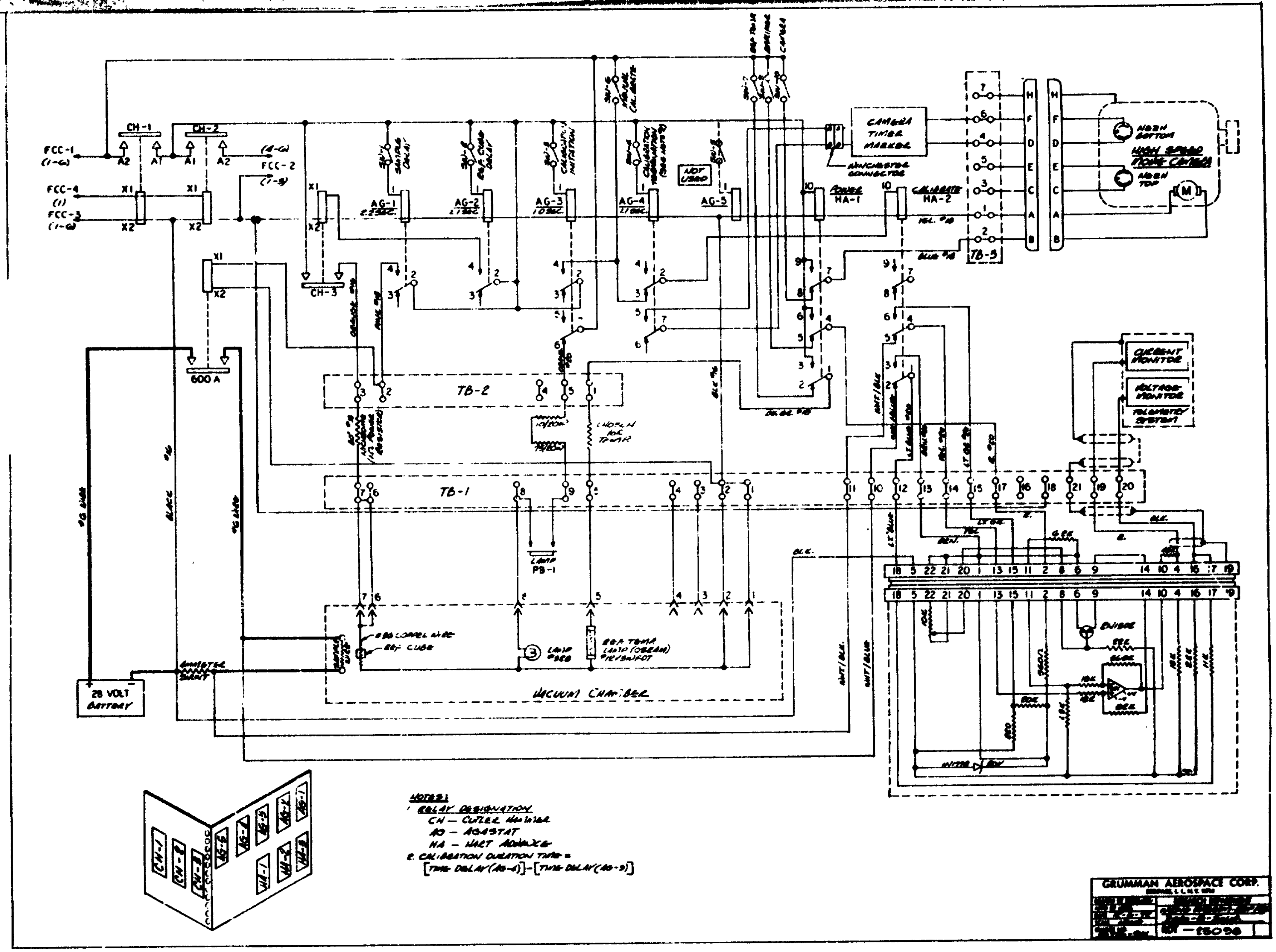

Fig. 3 Schematic Drawing of Electronic Circuit

command (approximately two seconds before actual drop), the following equipment is energized:

- High-speed camera
- Reference temperature wire
- Telemetry amplifier
- All timing relays

Approximately one second before drop, the calibration relay is energized. This establishes known signals for the two telemetry channels. The calibration duration is about 100 milliseconds, thus approximating expected experiment data (melt occurs in about 100 milliseconds for specimens under consideration). At the time the calibration is terminated, the NASA-supplied film timing mark generator is energized, providing a timing reference on the film for later data reduction.

About 0.2 seconds into the drop, the reference cube accelerometer is released, followed 0.1 seconds later by melting of the specimen wire. All timing is controlled by Agastat relays, Numbers 1-4 (see Fig. 3).

Vacuum Chamber

The vacuum chamber has a removable cover at one end (see Fig. 4). The cover has electrical feed-through currents to specimens of various thickness and length. The specimen holder is made of 1/4-inch copper buss bars, and the vacuum feed-throughs are of No. 10 threaded copper. The cover also includes an eight-terminal electrical feed-through capable of carrying 10 amps per terminal. This provides power for the observation lamp, reference temperature lamp, and reference cube release wire.

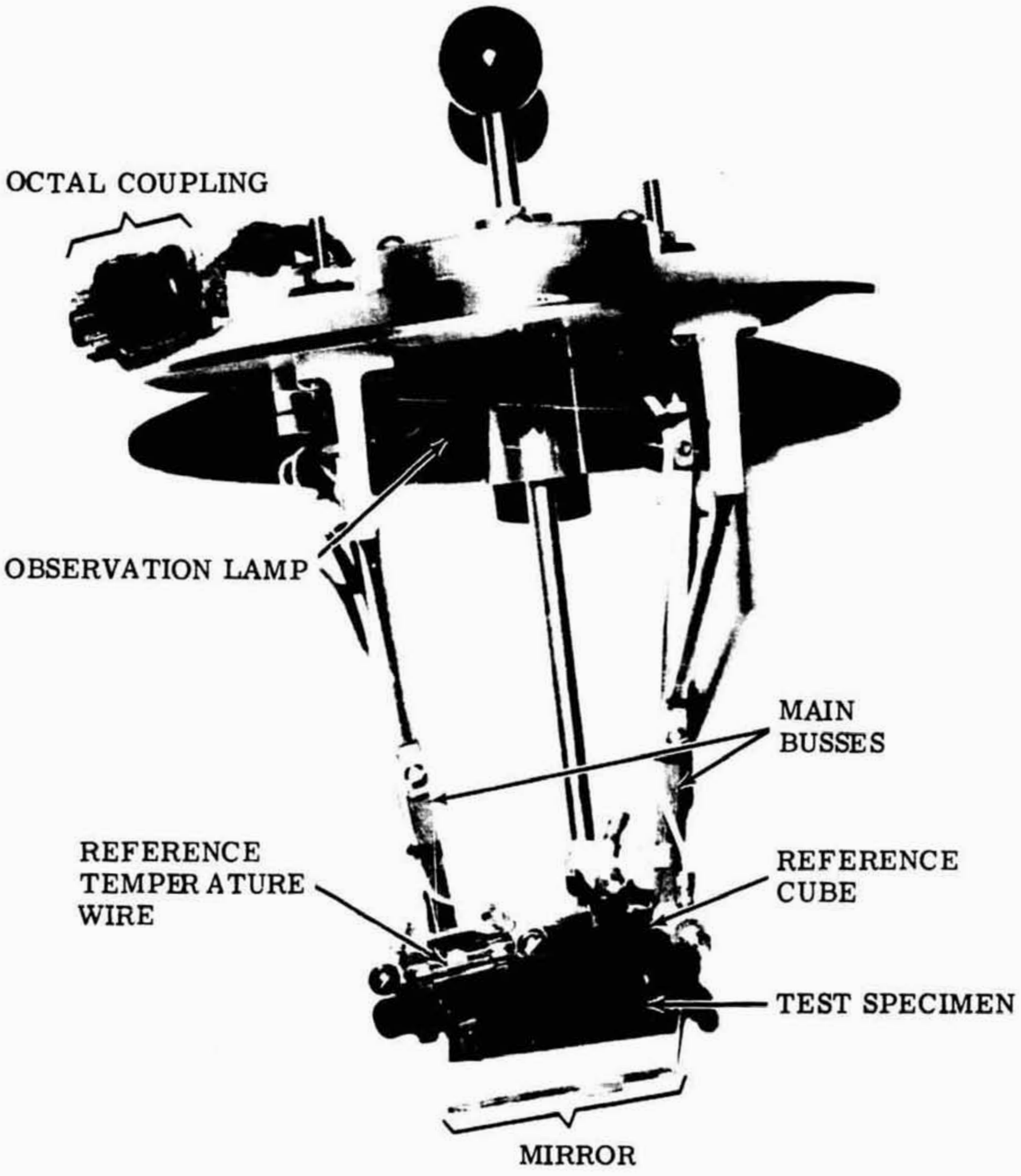

Fig. 4 Cover to Vacuum Chamber

Telemetry Amplifier and Signal Conditioner

Contained on this circuit board is a Zener regulated power supply, current monitor amplifier, and voltage dividers necessary for interfacing with the telemetry system. The schematic diagram is included in the system wiring diagram (Fig. 3); the physical layout is shown in Fig. 5.

The regulated supply provides power for the integrated circuit operational amplifier, as well as a voltage reference during the calibration interval. Calibration is accomplished by switching the input signal to the current amplifier to a known reference, thereby calibrating the entire telemetry channel including the current monitor amplifier. The voltage channel is calibrated in a similar manner providing calibration of the channel including all loading effects.

The circuitry for the current monitor necessitated the use of a biased output signal of about one volt. As this amplifier is energized two seconds before drop, this change in level (1 volt) indicates initiation of the timing sequence.

System Grounding

Owing to the low level monitoring signals and the high currents drawn by the melting wires, grounding has been carefully studied. The experiment has been divided into five blocks for grounding purposes. All grounds are returned to the ground buss located on the relay control panel, which provides a single ground point thereby minimizing ground loops.

Currents from the camera are directly returned to the ground buss and from there back to the power source. Current return lines from the reference temperature wire, observation lamp and reference cube release wire are tied together inside the vacuum chamber and returned to the ground buss. The ground return for the telemetry amplifier is tied to the low side of the specimen circuit ammeter shunt, and from the shunt returned to the ground buss on the relay control panel. The telemetry amplifier draws only milliamperes providing very small errors in data acquisition.

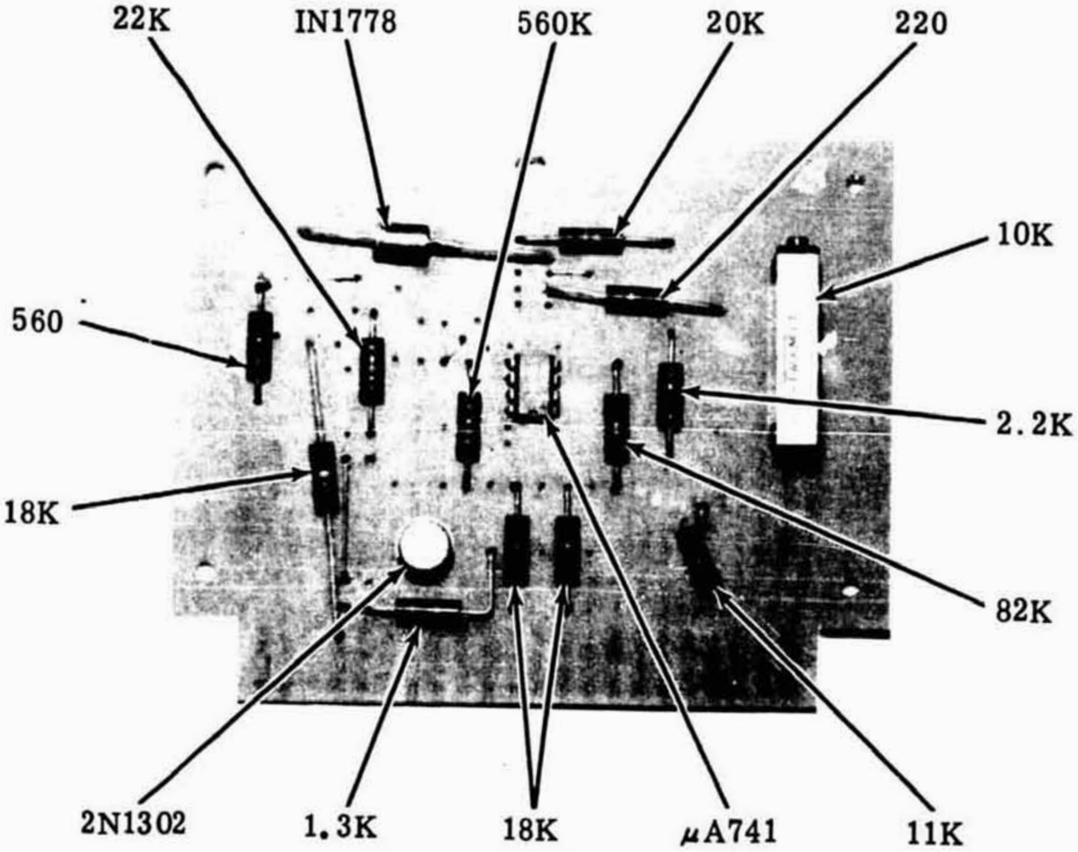

Fig. 5 Amplifier Circuit

EXPERIMENTS

Laboratory Experiments

Our initial wire melting experiments were carried out in a bell jar on several materials that were available in the laboratory. These are tabulated below with the wire diameter in centimeters. With sufficient power, it was possible to form spheres from all of these materials.

Metals	Alloys	Coated Wires	Other
Ag (0.025)	Nichrome (0.051)	Ni on Cu (0.015)	NiTi (0.160)
Ni (0.102)	Chromel (0.038)		
W (0.064)	Constatan (0.051)		
	SAE 1080 (0.102)		

The wide range of materials that were successfully melted indicates that the formation of unduloids and the resultant spheres is related to the process of power input and not the materials. Since even the highest melting metal, tungsten, formed spheres, it is expected that the wire melting experiment can be used to form spheres from any metallic conductor as long as it can be fabricated into wire or rod and sufficient power can be rapidly applied.

Since, at present, almost all zero gravity experiments are time-limited, it is instructive to consider what is the limiting size of sphere that we can form and solidify during this experimentation. If we assume the process to be the decay of a liquid column to a sphere, then the decay time for this process has been given by (Ref. 7):

$$\tau = \left(\frac{\rho}{\sigma}\right)^{\frac{1}{2}} R^{3/2}$$

where

ρ = density

σ = surface tension

2R = final sphere diameter

A survey of the literature indicates that ρ/σ has a value of about 0.06 for many metals at their melting points. Using this value, we have plotted the time to form spheres of various sizes, and this is shown in Fig. 6. The arrows indicate the limits on the sizes of spheres that could be formed in three seconds in the drop tower (5.1 cm) and in 12 seconds in a KC-135 flight ($\sim$ 13 cm) if sufficient power is available.

It is next of interest to consider how large a sphere we can solidify in the time available if we assume it is molten at the instant of achieving zero g. This has been done for two cases (Ref. 8), both of which assume the sphere is a pure metal at its melting point. In the first case, all the heat of fusion is rejected by radiation, and evaporation is neglected. The second case is for a very volatile element and assumes radiation heat transfer is small. Figure 7 presents some of the results for different metals. Consideration of Figs. 6 and 7 shows that in the time available in the drop tower we can form very large molten spheres, but they will not be completely solidified before the restoration of gravity. If large spheres are formed, then only the outer shell will have a chance to solidify before impact. The structures resulting from such a solidification are discussed under Microstructural Analysis.

When performing the experiment in a bell jar in the laboratory, using ac heating, it was observed that a threshold voltage (or power) exists below which no spheres are formed. Figures 8 and 9 show examples of this for chromel and nickel wire. As the

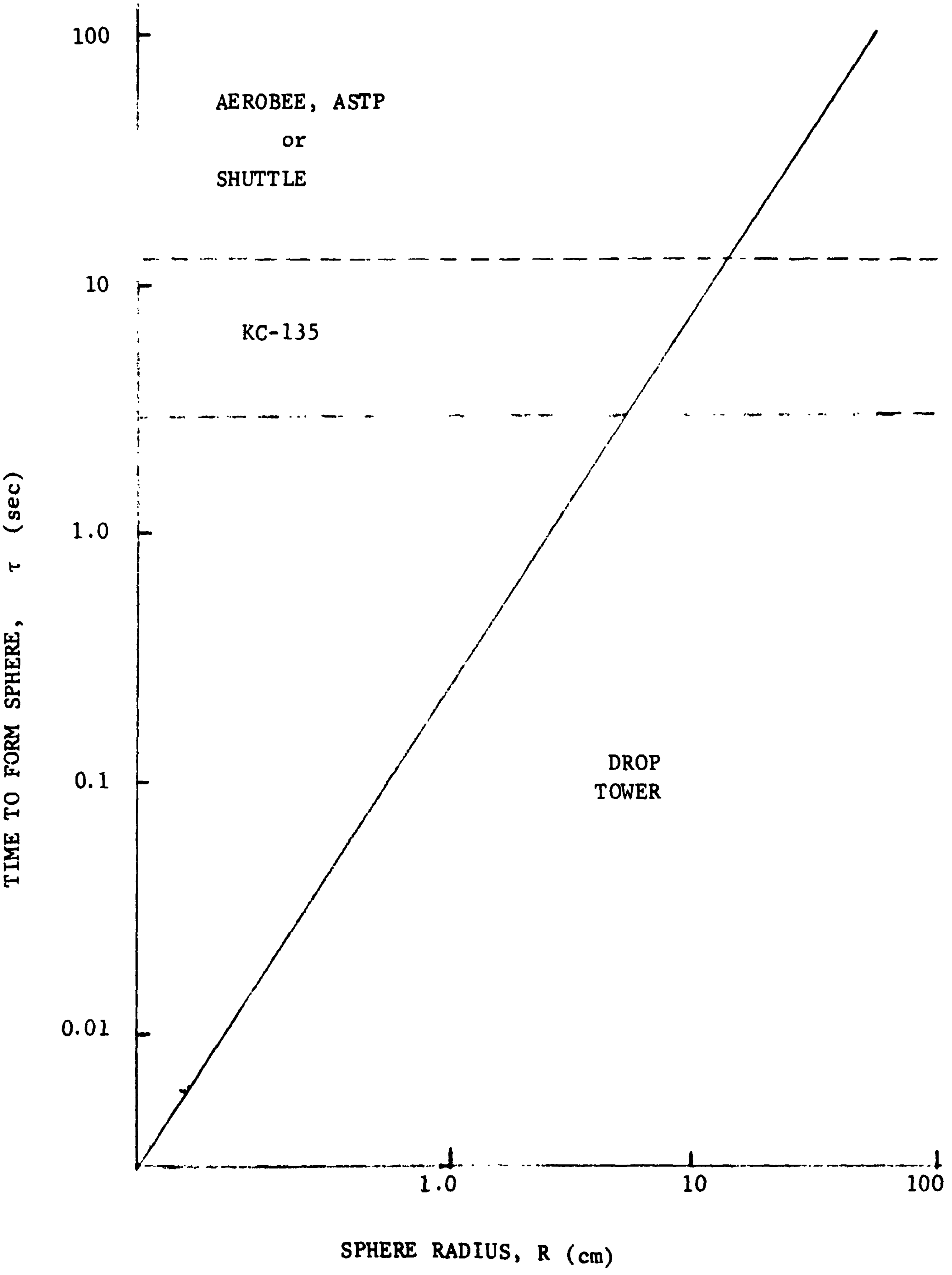

Fig. 6 Time to Form a Sphere of a Given Radius

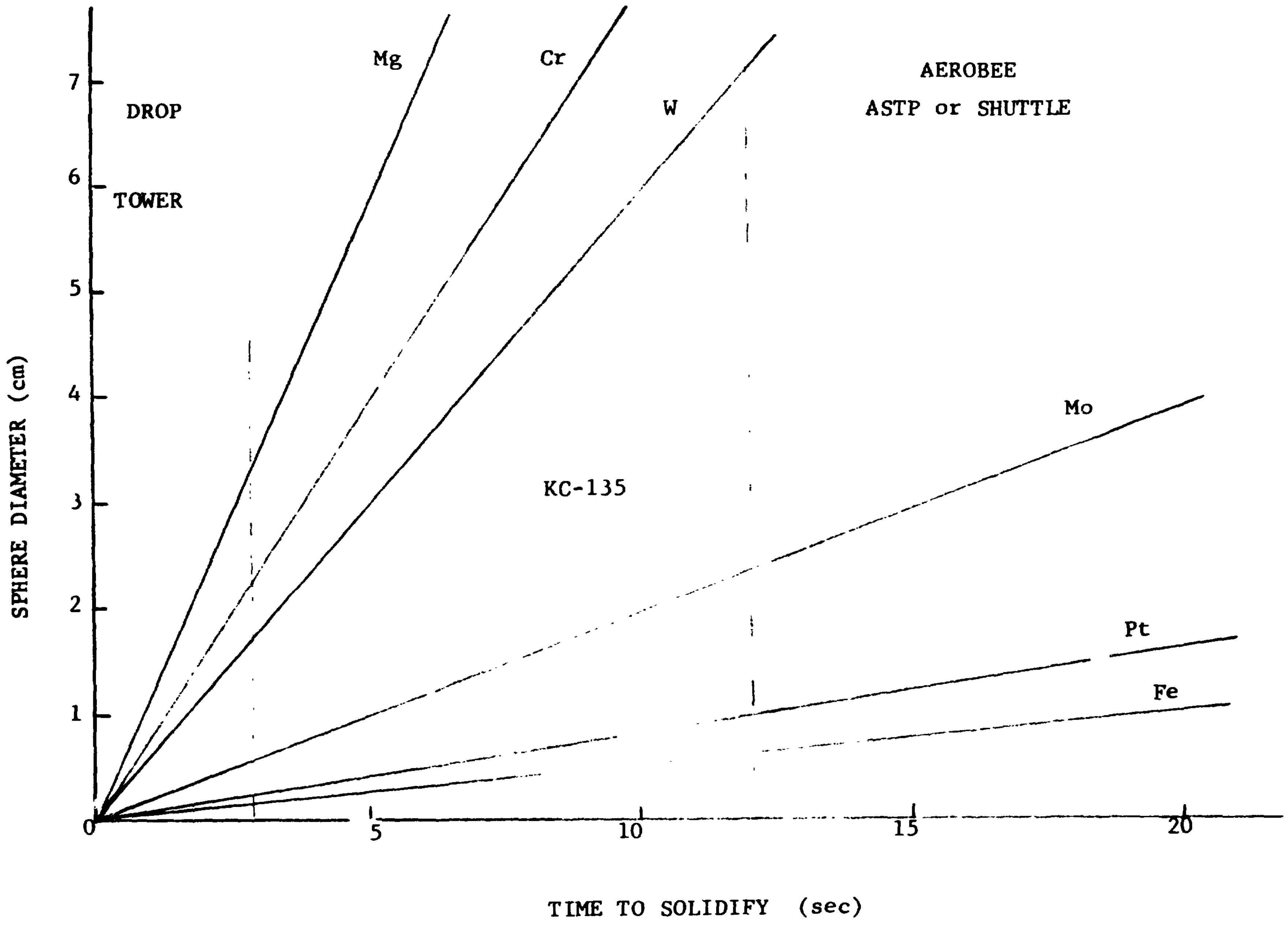

Fig. 7 Time to Solidify a Sphere of a Given Diameter

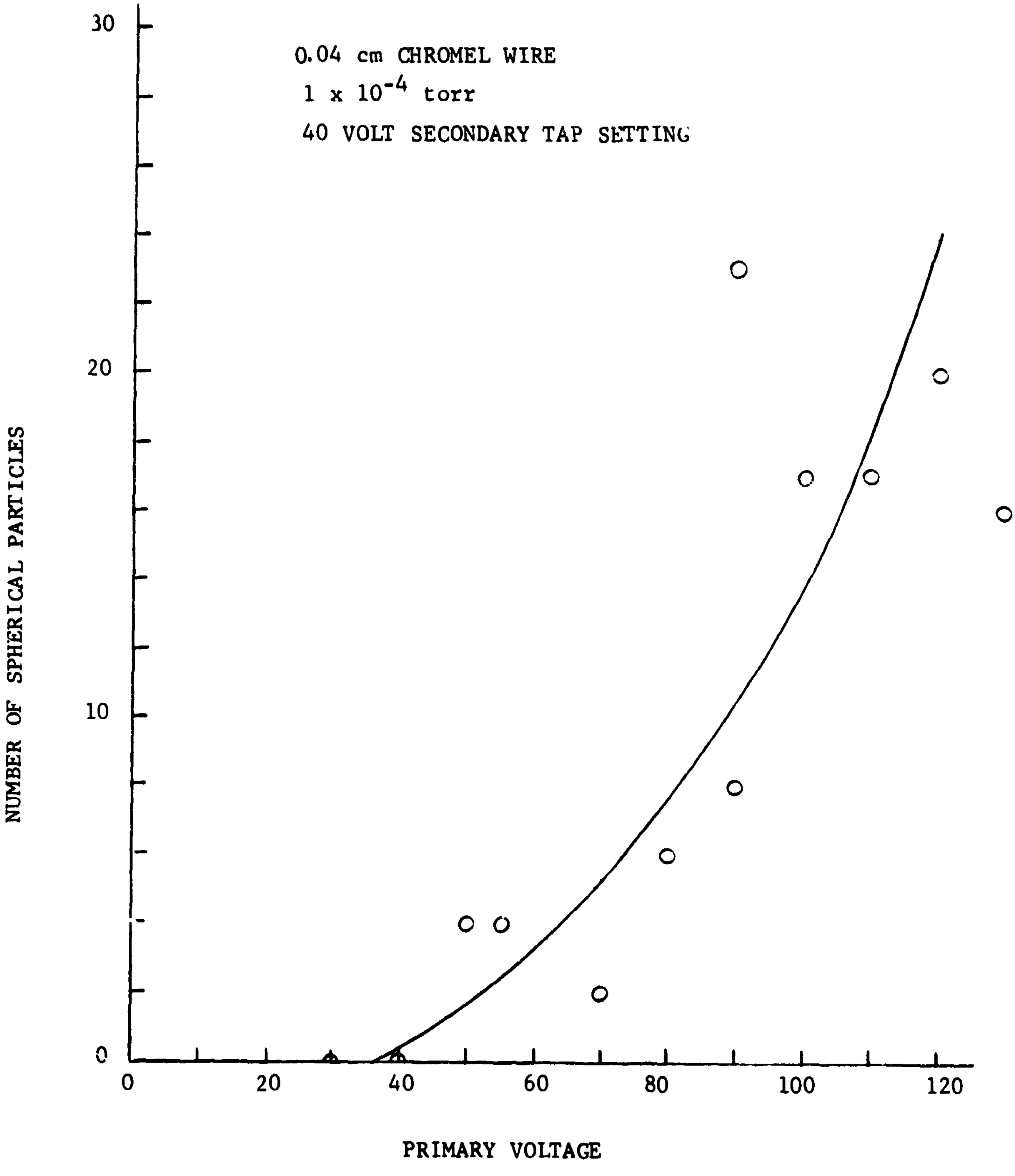

Fig. 8 Threshold Voltage for Sphere Formation Using Chromel Wire

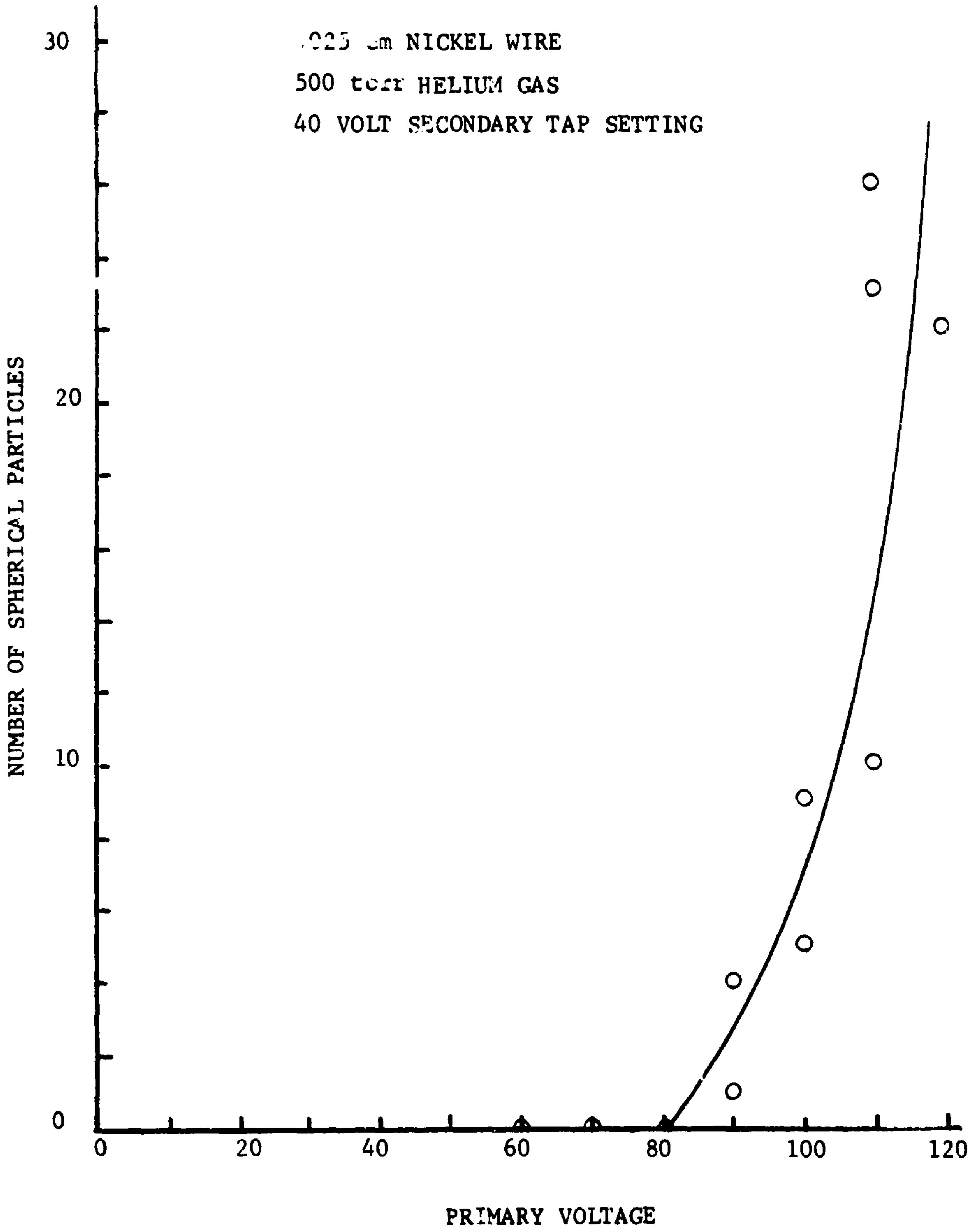

Fig. 9 Threshold Voltage for Sphere Formation Using Nickel Wire

voltage increases, the number of spheres formed rises rapidly. Since the sphere diameter remains relatively constant, this result indicates that more of the length of the wire forms spheres. As expected, increasing the wire diameter increases this threshold voltage; however, the shape of the curve remains the same.

The results shown in Fig. 8 are for a vacuum of 10^{-4} torr. If the pressure in the chamber is increased, the threshold voltage also increases, as shown in Fig. 9. The curves in Figs. 8 and 9 have the same shape, but the number of spheres formed increases more rapidly with voltage at the higher pressure.

Bench Test Experiments

The apparatus underwent a thorough bench test prior to shipping to Marshall Space Flight Center. The chamber was connected to a vacuum station containing a 4-inch diffusion pump and a roughing pump (see Fig. 10). The one leak found during these tests was in the "O"-ring slip seal for the ion gauge. This seal was eliminated by welding the gauge flange directly to the chamber. The gauge was then bolted again to the flange.

During the vacuum check runs, the chamber was baked out for several days using an electric blanket. By the time the first specimen was fired in the chamber, we were able to consistently reach vacuums of 1×10^{-4} torr in the chamber. About 15 to 20 minutes were required to reach this vacuum level.

Nine complete bench runs were made. Five of these were recorded with color film and one in black and white. No film record was made on the remaining three. These runs showed the need for several minor changes. The series resistance for the chamber viewing lamp was decreased, the series resistance to the reference temperature bulb was selected and installed, and, finally, the

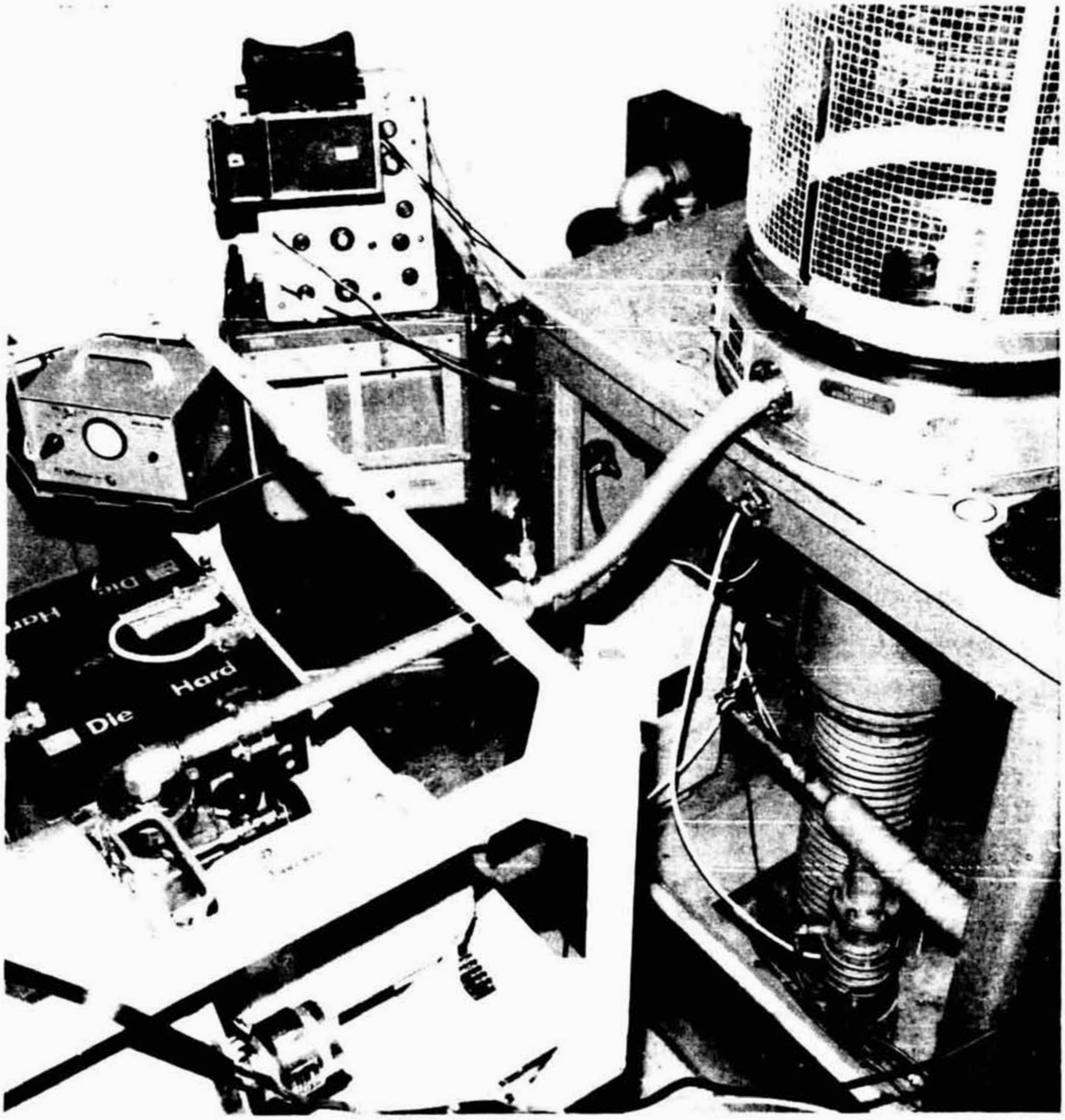

Fig. 10 Photograph of Vacuum Pumping Station

firing sequence was modified because it was seen from the strip chart records that the camera and reference cube circuits both affected the current and voltage of the specimen circuit. The sequencing was set up, therefore, so that the secondary circuits were activated prior to activating the primary specimen circuit. This sequencing is shown in the service manual (Ref. 9). The developed film confirmed the operation of the specimen melting circuit and the reference temperature lamp. The latter was set at a reference temperature of 1450°C with an optical pyrometer.

The bench tests completed the testing at Grumman. The rig was at this point crated and shipped to MSFC to begin the testing in the drop tower.

Drop Tower Experiments

The drop tower facility at MSFC is described in Ref. 1. It consists of a cylindrical chamber eight feet in diameter and ten feet long where the experiment package, described in the Hardware Design and Development Section of this report, is allowed to float free during a 300 foot drop. The chamber has a hemispherical cap on the bottom. This cap houses a bank of NiCd batteries used to power the telemetry transmitter and other accessories during the drop. The top of the chamber is a cone and houses the pressure spheres used to thrust the entire chamber (called a drag shield) toward the ground. This thrust overcomes the air drag of the drag shield and extends the length of zero g test time. The entire setup is shown in Fig. 11 in a schematic prepared by NASA.

Two series of drops about one month apart were carried out in the drop tower. Seven drops were made in the first series and ten in the second. Table 1 lists materials and size of specimen for each drop.

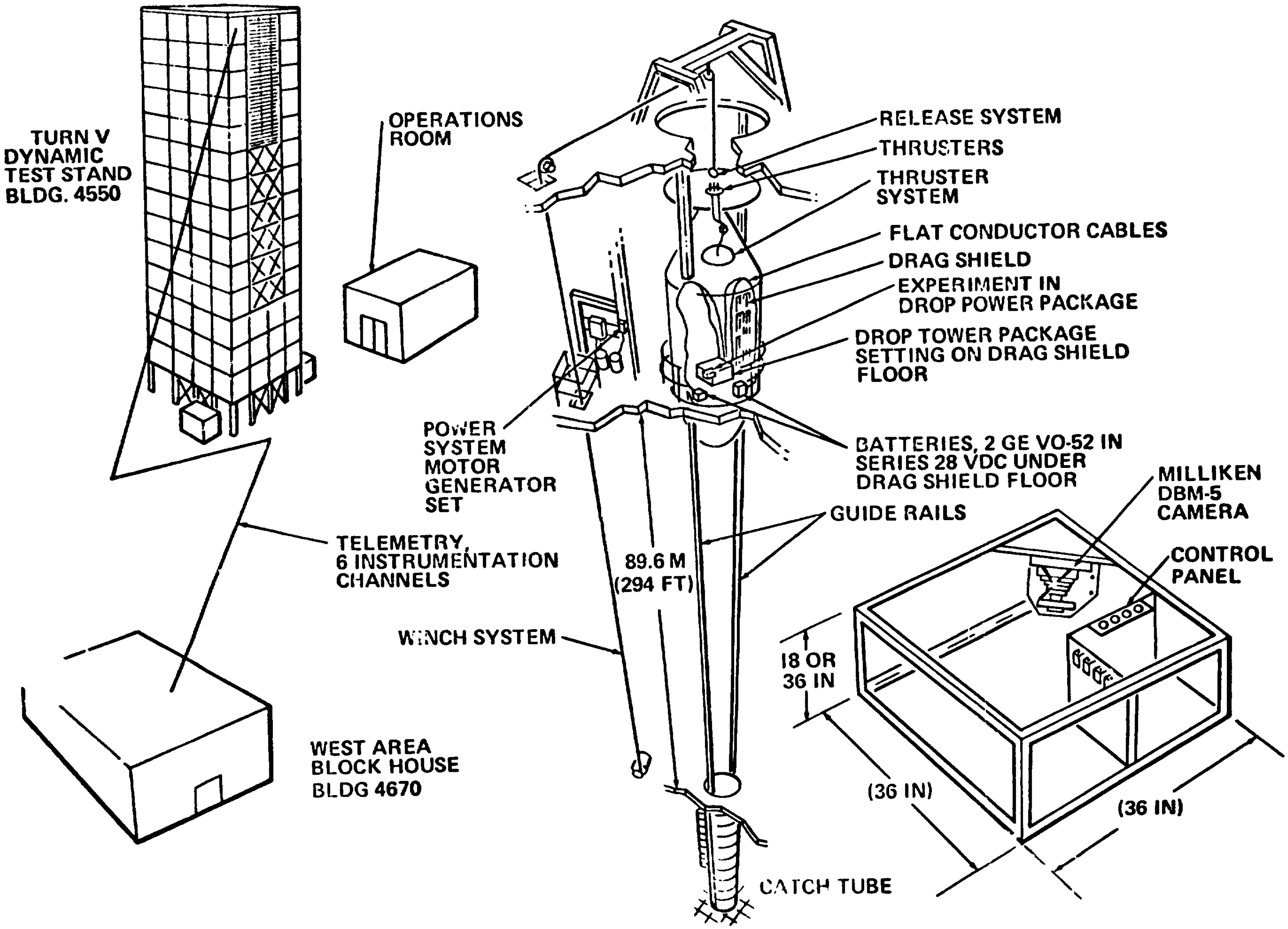

Fig. 11 Schematic of NASA Drop Tower

TABLE 1 MATERIALS AND SPECIMEN SIZES FOR DROPS

Run No.	Material	Diameter (cm)	Length (cm)
T1	Nickel	0.127	6.03
T2	Nickel	0.051	6.03
T3	Nickel	0.051	6.03
T4	Steel	0.051	6.03
T5	Steel	0.102	6.03
T6	Nickel	0.102	6.03
T7	Steel	0.051	6.03
2T1	Nickel	0.318	10.16
2T2	Nickel	0.318	7.62
2T3	Nickel	0.318	5.08
2T4	Nickel	0.183	7.62
2T5	Nickel	0.157	7.62
2T6	Nickel	0.117	4.45
2T7	Nickel	0.117	3.81
2T8	Nickel	0.117	2.54
2T9	Nickel	0.117	3.81
2T10	Nickel	0.051	2.54
2T11	Nickel	0.051	5.08

In the first series of drops, spheres were formed in four of the seven drops. Only in drops T1, T5, and T6 (where a heavy wire was used) did spheres fail to form. Drops T6 and T7 had only 14.5 volts in the specimen circuit (one battery), but even with reduced voltage, Run T7 (0.051 cm dia steel wire) gave spheres.

In only one drop of the second series were spheres successfully formed. All of the runs made in the second series were simulated in the laboratory prior to entering the drop tower. Spheres were formed in most cases. In the Laboratory Experiments section we discussed the threshold power needed for sphere formation. The laboratory tests were carried out in a vacuum of 10^{-4} torr and in an inert gas (argon) at atmospheric pressure. In both cases, there was a threshold power, but it was not markedly different.

Subsequent to the second series of drops, laboratory experiments were conducted using "Die Hard" batteries, 0.10 cm Ni wire five cm long, and three pressure levels: diffusion pump vacuum ($\sim 1 \times 10^{-4}$ torr), roughing pump vacuum ($\sim 5 \times 10^{-2}$ torr), and atmospheric pressure. At the highest and lowest pressures, spheres formed, although at atmospheric pressure they were oxidized. At the intermediate pressure, no spheres ever formed; the wire always broke into segments.

Thus, the explanation for the nonformation of spheres in the second set of drops may have resulted from the outgassing or leaking of the chamber up to a critical pressure level between valve-off and dropping. The pressure-voltage-sphere formation tendency will be investigated more fully in the next phase of this work.

ANALYSIS OF DATA

Telemetered Data

Telemetered data for sample current and voltage were obtained in the form of chart recordings. The chart paper was run at 25.4 cm per second. The calibration sequence permitted calibration of the overall instrumentation and chart recorder system.

The time history for voltage and current was sampled at 0.254 cm intervals (corresponding to 0.010 second intervals). The data were essentially digitized by measuring the time history from the reference line to an accuracy of ±0.040 cm.

Measured voltage and current were used to calculate instantaneous resistance and power as a function of time. The power curve was integrated to develop the energy curve as a function of time. These graphs appear in Figs. 12 and 13. Sample calculations are included in the Appendix.

The runs that produced spheres were Runs T2 and T3 (0.051 cm diameter nickel) and Runs T4 and T7 (0.051 cm diameter steel). The majority of the data reduction effort was directed to analyzing these four runs.

One must remember that resistance calculations result in qualitative results, assuming uniform temperature distribution and an equivalent length equal to the set length. In addition, no attempt has been made to compensate for hookup wiring resistance, contact resistance, heating of contacts, etc. Energy calculations are, therefore, subject to large errors.

Discussion of Nickel [Runs T2 and T3 (0.051 cm dia)]

The two runs on 0.051 cm diameter nickel were essentially duplicates. They were run on different days but with the same

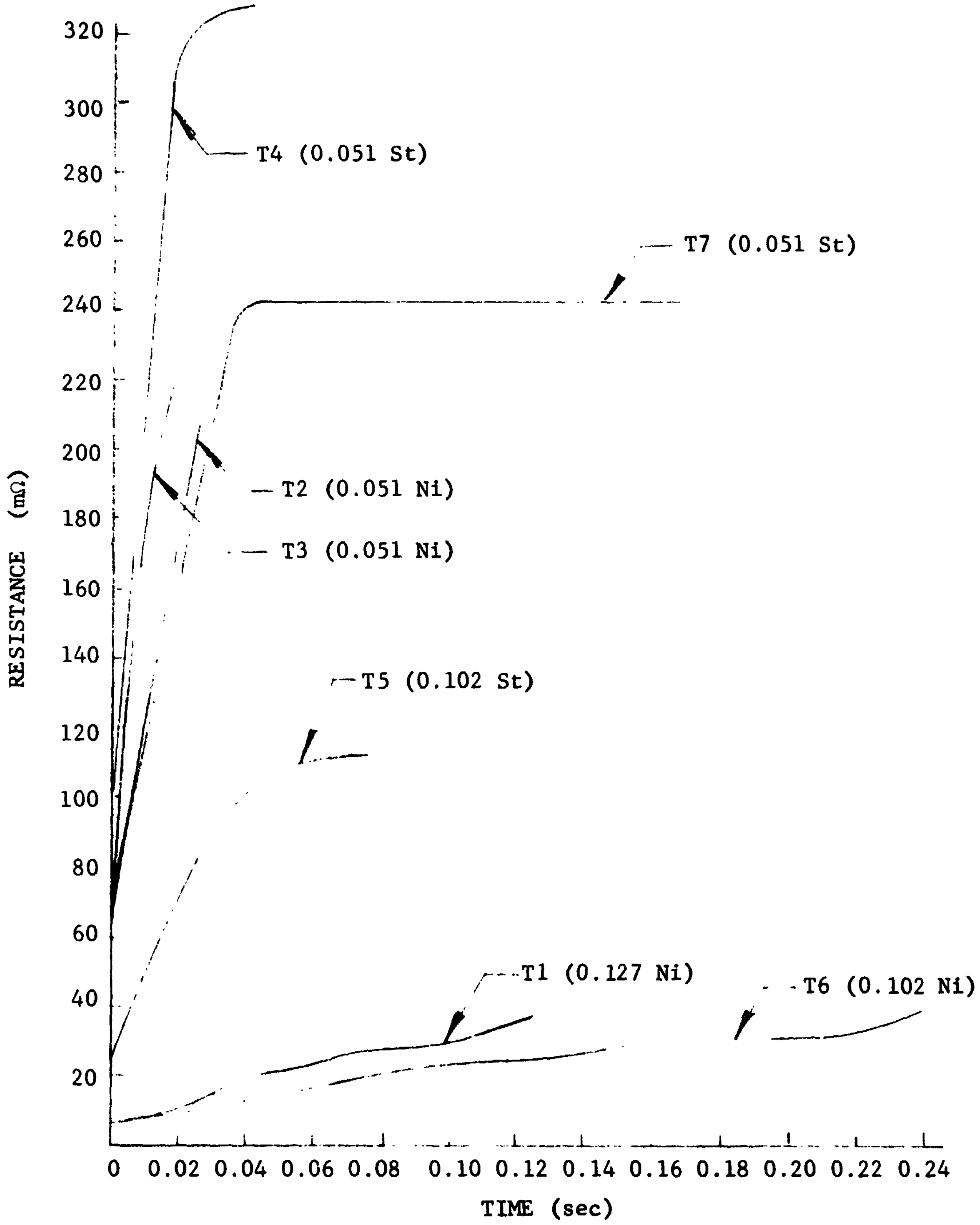

Fig. 12 Specimen Resistance Versus Time for First Series of Drops

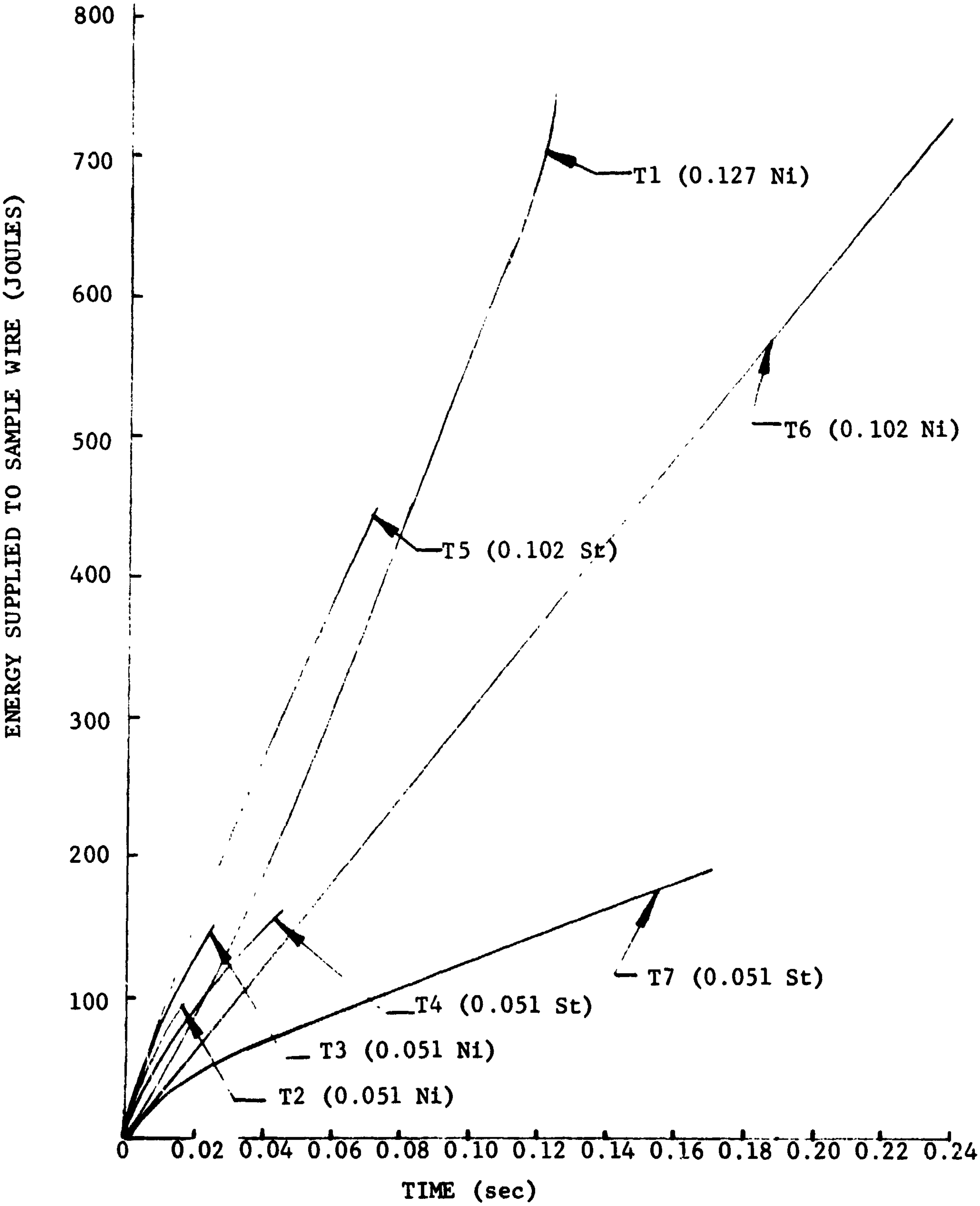

Fig. 13 Energy Versus Time for First Series of Drops

battery supply, etc. The results were very similar, providing almost identical final hot resistances (0.2250 Ω - Run T2, 0.2285 Ω - Run T3).

Resistances determined for nickel at room temperature (cold) were not in agreement with published data. It was felt this was due to the difficulty in reading voltage and current during the initial rapid rise in both values. For this reason, the published values for resistance at 20°C were used in the calculations. Temperature calculations for nickel at the instant of breaking (hot) using the final resistances computed from the telemetry resulted in melting temperatures of 1743K for Run T2 and 1753K for Run T3. These temperatures agree well with the published melting temperature for nickel of 1728K.

Discussion of Nickel [Run T1 (0.127 cm dia) and Run T6 (0.102 cm dia)]

The calculated final temperature in Run T1 was 1833K, which was in reasonable agreement with the published melt temperature. This specimen did not provide the desired samples but broke into large lengths. From this action, it seems the final temperature should have been under the melt temperature.

Run T6 was conducted with reduced voltage and calculations give a low final temperature (1243K). One of the two nickel/cadmium batteries was used, and voltage to the specimen was 14.5 volts as compared to 29 volts for Runs T1 through T5. The high speed camera revealed a slow heating rate (0.075 seconds from visibility to failure as compared to 0.025 seconds for Run T4) and an uneven temperature distribution. The temperature distribution is the probable reason for the low calculated temperature. As stated earlier, without correcting for the temperature gradient, analytical calculations are not possible.

Discussion of Steel

The resistance versus time curves for steel show a nonlinear behavior with flattening of the resistance of the steel versus time (see Fig. 12). Published data for the steel used are included in Fig. 14. Note that there is a change in the slope of the resistivity versus temperature curves on heating above the eutectoid temperature, 996K. The change in resistance versus temperature is so small at temperatures above 1073K that small errors in calculated resistance can cause very large errors in temperature.

As an example, consider a ±5 percent error in calculating the resistivity of steel at 1273K. Resistivity would vary from 113.5 to 125.05 microhm centimeters. This corresponds to a temperature range of from 1063-1626K, an error band of +35.3 to -21 percent, corresponding to only a ±5 percent change in resistivity. It is felt, therefore, that calculations of resistance for steel will have no value in obtaining a final temperature.

No attempt was made to reduce any of the telemetry data from the second series of drops. We can summarize the results from the first series as follows: In all of the energy calculations, it is obvious that unless the heating is very rapid, resulting in a uniform temperature distribution, large errors ensue. Steel, having an extremely nonlinear resistance versus temperature, cannot have melt temperature calculated from telemetered data to any appreciable degree of accuracy. Nickel, on the other hand, has a linear resistance versus temperature characteristic yielding quite consistent results.

A major problem exists trying to compute specimen temperature by this calculation method. The method assumes a uniform temperature across a known length and thermal equilibrium, neither of which applies to this experiment. It is felt that the nickel most

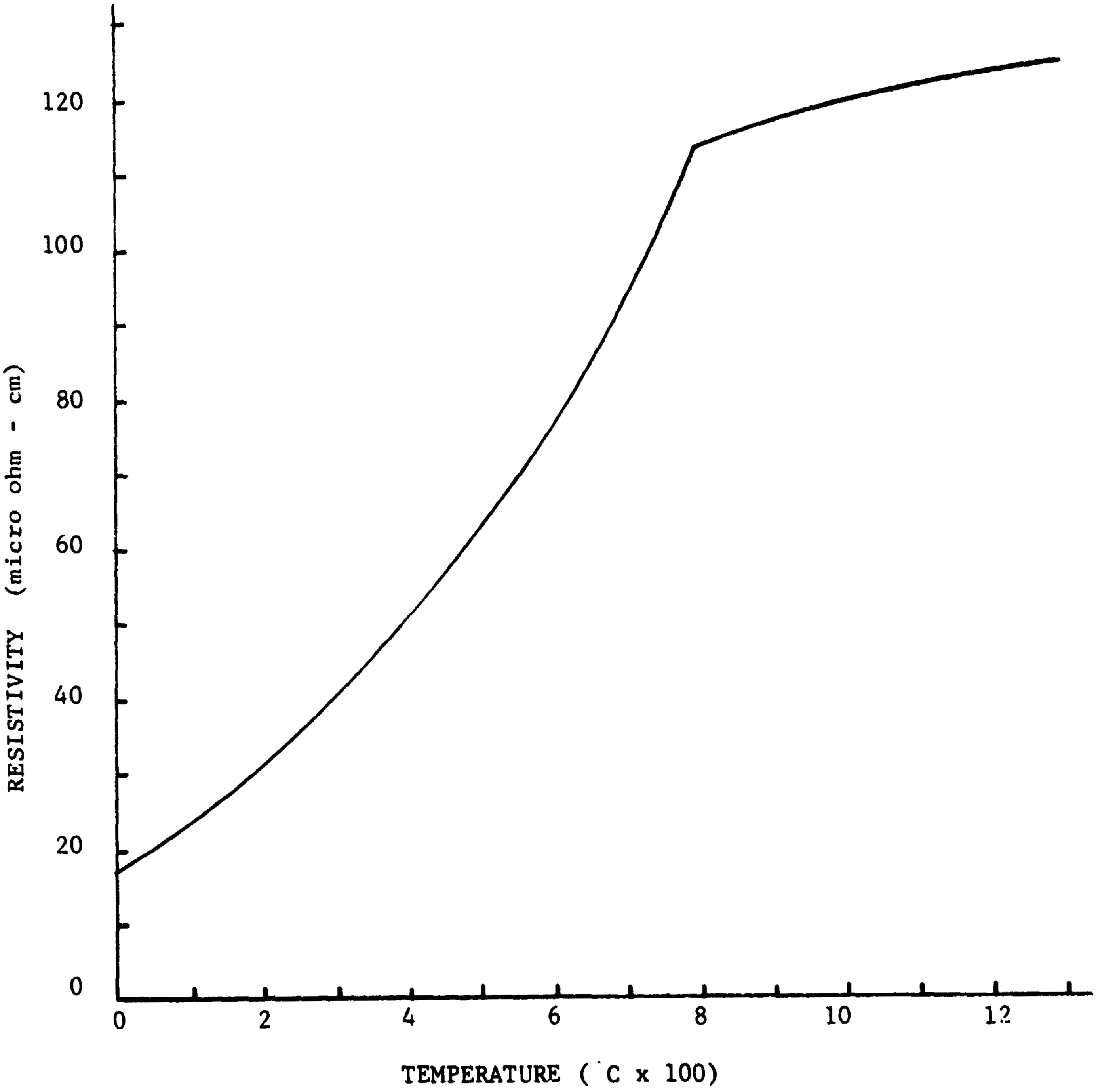

Fig. 14 Resistivity of Steel Versus Temperature

closely approximates the requirements due to the close agreement from run to run.

The relatively large percentage error for low currents should be avoided through a change in either instrumentation gain or chart recorder gain when low currents are expected.

Temperature Measurements

The temperature-time history of a sample in a melting and solidification experiment is of primary importance. In this experiment, temperature measurement is difficult because of the rapidity of heating and cooling and because of the movement of the sphere following its formation. To follow the specimen and record its temperature-time history, a photographic technique using a high-speed movie camera was developed (Ref. 10).

Because color film is highly nonlinear, it is impossible to make absolute temperature measurements without a standard. The use of a standard to produce reference temperatures in the apparatus allows for the necessary corrections on moving from the bench test calibration to the drop tower chamber.

The photometric relation is such that the energy density reaching the film, E_λ, is proportional to the Planck blackbody radiation function, F, the exposure time, t, the wire emissivity, ϵ, a geometrical factor, G, and the film bandwidth, $\Delta\lambda$, and can be expressed as:

$$E_\lambda = F \cdot t \cdot \epsilon \cdot G \cdot \Delta\lambda \ .$$

Calibration curves for the film were generated in the laboratory using a Bolex model H16M 16mm motion picture camera and Kodak Ectachrome EF film, type 7242, from a single batch (No. 72427790BC). The emulsion of this film is balanced for 3200K tungsten light with an ASA rating of 125. Tungsten wires approximately 0.006 cm and 0.010 cm in diameter were photographed at various temperatures from 1173-2573K. The wire temperature was checked before and after filming with an optical pyrometer. Because of the high intensity of the emission from the wires at these temperatures, the camera was run at 64 frames per second at an aperture setting of f/22. A lens distance of 55.88 cm was maintained throughout, and the film was developed using the standard Kodak ME4 process.

The developed film was then analyzed with a Joyce Lobel microdensitometer. The microdensitometer was set with a lateral magnification ratio of 500 to 1 and a spot size of 0.02 square millimeters. Separate traverses were made across each frame for the three wavelengths studied (4400, 5300, and 6300Å). These correspond, approximately, to the characteristic wavelengths of the three emulsions. The traces for each wavelength and each frame were calibrated for optical density by inserting a precision neutral density filter in the microdensitometer beam. The optical density of the wire center, for each wavelength and frame, was then calculated and plotted as a function of Planck's blackbody radiation function, at the appropriate temperature. These calibration curves were then utilized, in conjunction with the internal reference wire in the drop tower package, to yield specimen temperature data. This data required a further correction for the spectral emissivity of the specimen material relative to that of the tungsten calibration material.

The experimental sequence in the drop tower was to standardize the reference temperature wire prior to each drop, typically 1773K, with an optical pyrometer. The drop tower films, taken at a speed of ~ 300 pictures/second on a 16mm Milliken camera, were then analyzed for the three wavelengths, and both the specimen wire and reference optical densities were monitored. For a given wavelength, the drop tower densities of each frame were compared with the previously generated calibration curves. The reference temperature was adjusted to the calibration curve, and the unknown temperature was then read from the calibration curve. This cross-reference technique corrected directly for such nonlinear film responses as development variation, exposure time, geometrical differences, and the band-pass filters utilized.

This left only one additional photometric correction, which was the previously mentioned spectral emissivity. This proved to be somewhat of a problem as the spectral emittance of the test materials is likely to vary with wavelength, temperature, and surface condition. The emissivity correction is the final correction and directly alters the apparent specimen temperature, and consequently, is a critical adjustment. Further work will have to be done to improve this correction. Despite these problems, however, the brightness temperature technique gives reasonable values and is fully capable of operating within the experimental time constraints.

Several methods are available to obtain more accurate temperatures. One obvious technique would be to determine emissivity of the materials of interest at the three wavelengths and as a function of temperature. This technique has already been developed elsewhere and merely requires application to materials of interest. Another approach would be to make use of the multispectral information from the three emulsions to measure color temperature instead of brightness temperature. This would cancel all but second order emissivity changes with wavelength and temperature. Color temperature measurement, however, is more sensitive to errors in photometry of the film because the blackbody emission is an exponential function of wavelength for our case. A solution to this problem would be to use a color balance filter, which would attenuate the strong red emission but not the blue. This would require that the complementary filter be used for visual viewing to restore true colors. The color balance filter would have the added advantage that all three emulsions could be utilized for increased accuracy, whereas for the present work, only two of the three wavelengths could be utilized for any given frame.

Figure 15 shows a typical temperature-time history for drop tower Run T3 (0.051 cm dia nickel wire). Shown are the calculations for the 0.530μm and 0.630μm wavelengths. These curves qualitatively follow the idealized temperature-time heating and cooling curves of a pure metal, shown in Fig. 16. The initial rapid temperature rise is due to resistance heating of the solid, and the plateau, or thermal arrest, is due to the time and heat required for melting. The sample is now a liquid column and superheating begins as the column goes unstable. Unduloids are formed and these in turn spheroidize. At this point, the circuit is opened and cooling ensues. Cooling progresses until the solidus temperature is reached, and then there is a thermal arrest due to the heat of solidification.

Figure 6 shows that the time required to form a sphere of approximately 0.051 cm is about 0.003 second. This is close to that shown in Fig. 15 for the film technique. Figure 7 indicates that the time to solidify a sphere of this diameter while under free fall conditions is significantly longer, of the order of seconds. This, too, is recorded in the film temperature-time history data (Fig. 15) with the limitation that sampling was stopped well before solidification was completed. It is clear, then, that qualitatively the film technique offers confirmation of the ideal-

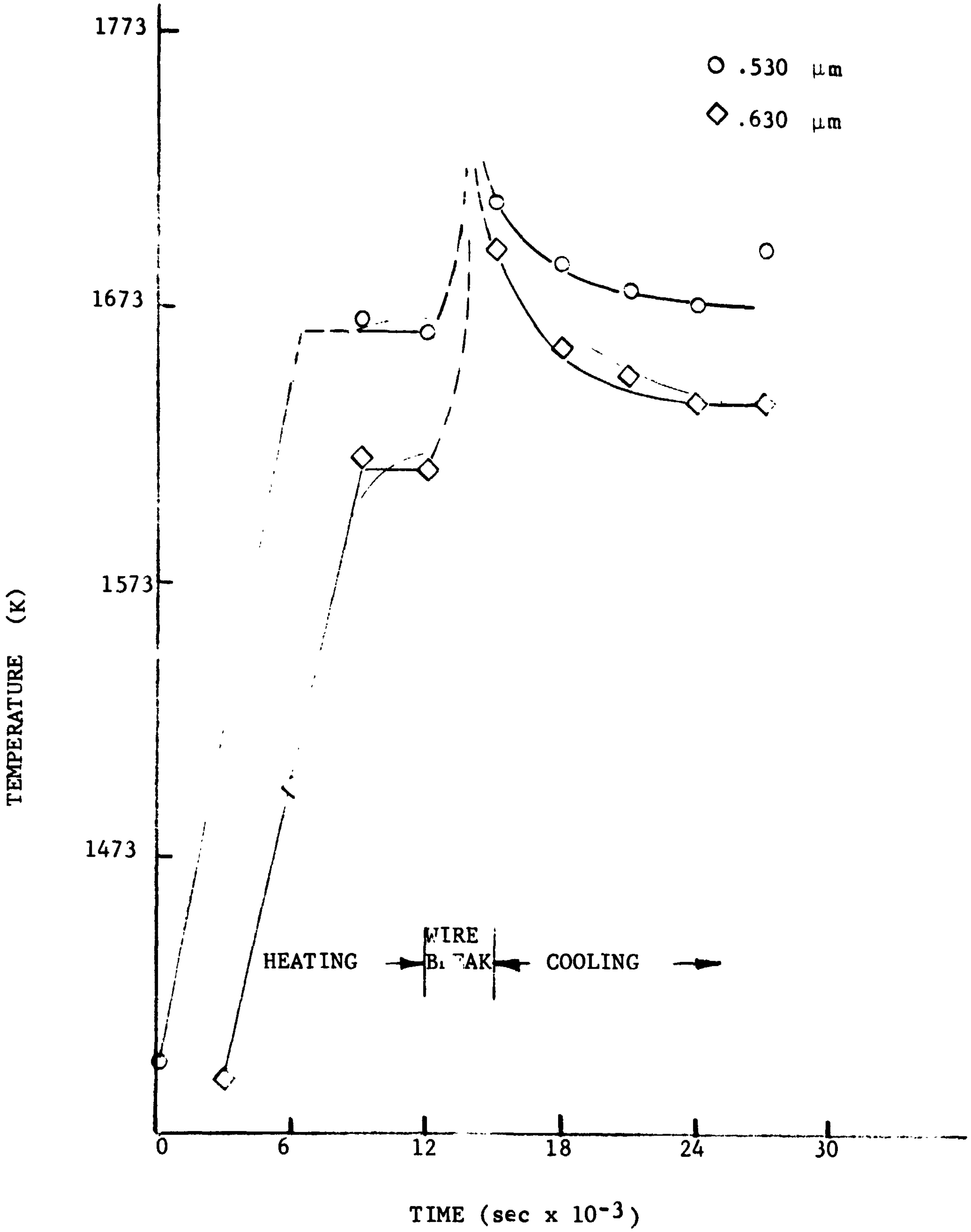

Fig. 15 Temperature-Time History for 0.051 cm Nickel Wire

ized temperature-time history, and although the quantitative agreement is reasonable, we feel that we can improve it.

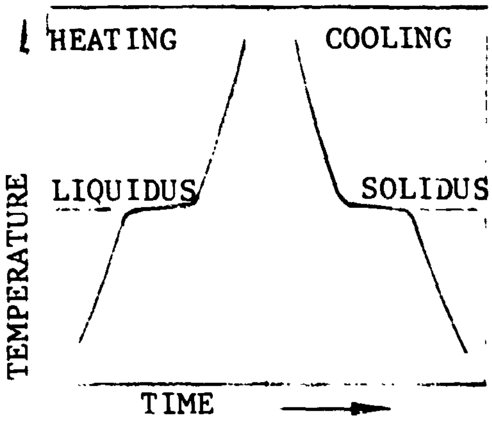

Fig. 16 Idealized Temperature-Time Heating Curve for a Metal

Microstructural Analysis

This section describes the surface and interior microstructures of both the laboratory and drop tower specimens and their experimental conditions and material parameters. Specimens were examined for specimen geometry, surface morphology, and interior microstructure. Each of these is discussed.

Specimen Geometries

Samples of both pure nickel and 1090 steel experienced local or segmented failures (Fi 17). The microstructure of these samples indicated that the bulk of the samples had been heated well into the grain growth region, but without melting. Melting was localized to the segment surfaces and some grain boundaries. The former might be attributed to "skin effect," whereas the latter might be attributable to chemical, morphological, or electrical heterogeneity associated with the specific grain boundary.

The surface morphologies indicated a melting process that initiated in the grain boundaries. This was misleading because the extent of melting could be overestimated if only a surface analysis was conducted.

Fig. 17 Local or Segmented Failures

The bulk interior morphology was an array of large equiaxed grains with appreciable numbers of annealing twins. This morphological array is clearly the result of a solid state process (grain growth or recrystallization) and not due to solidification from the melt. We may then unambiguously conclude that these samples remained solid through the experiment.

The final droplet shape after the unduloid formation and separation is dependent on a number of variables, such as liquid temperature and local temperature distribution, time in the liquid state, sample contamination, sample release velocity, emissivity, heat of solidification, size of the chamber, and perhaps many more.

We will not pursue each variable specifically; however, their overall effects may be grouped into the following considerations: sample velocity upon reaching the chamber wall, specimen viscosity upon reaching the chamber wall, and the time of solidification. Utilizing this generalization, an interesting analogy can be made, with reference to work conducted in the study of liquid wetting (Ref. 11). In this work, a drop of liquid at constant temperature, and therefore of constant viscosity as $\eta = f(T)$, is placed on substrate at the same temperature. The droplet of wetting liquid is then watched as a function of time, and the droplet shape sequence is shown diagrammatically (see Fig. 18).

If we now consider an analog to be somewhat consistent with our experiment, we must consider viscosity the primary variable, and we must approximate that the time available for solidification on impact will be small and, therefore, relatively constant (constant $\sim$ t). We may now present a new sequence of specimen geometries in Fig. 19. It is clear that this new geometrical sequence is similar to that shown in Fig. 18 (Ref. 11). It appears, then, that the observed macroscopic geometrical shapes noted are related most directly to specimen viscosity. Decreasing viscosity or increasing velocity will result in a specimen shape comparable to that shown in Fig. 19.

Some samples have a solidified shell prior to contact with the chamber walls. In this case, if the shell is of sufficient strength to withstand the impact, the specimens will remain spherical or only be partially flattened, and the solidification pattern will not emanate from the region of the flat.

In general, it was found that the degree of sphericity of the drop tower samples was considerably greater than that of the laboratory samples. This reflects the increased solidification

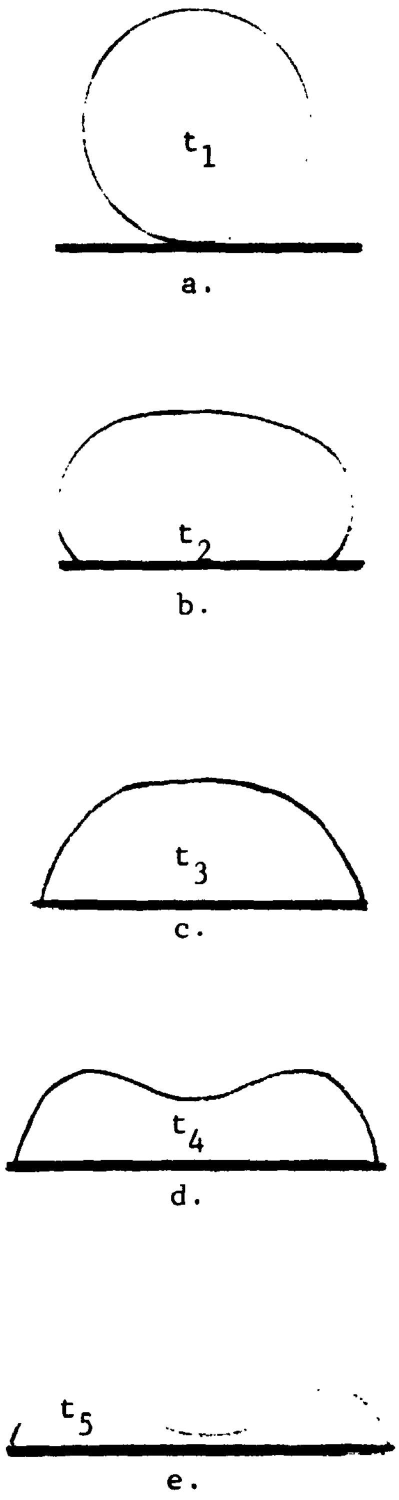

$\eta = f(T) = \text{const}$

$t_{i+1} > t_i$

Fig. 18 Droplet Shape as a Function of Time

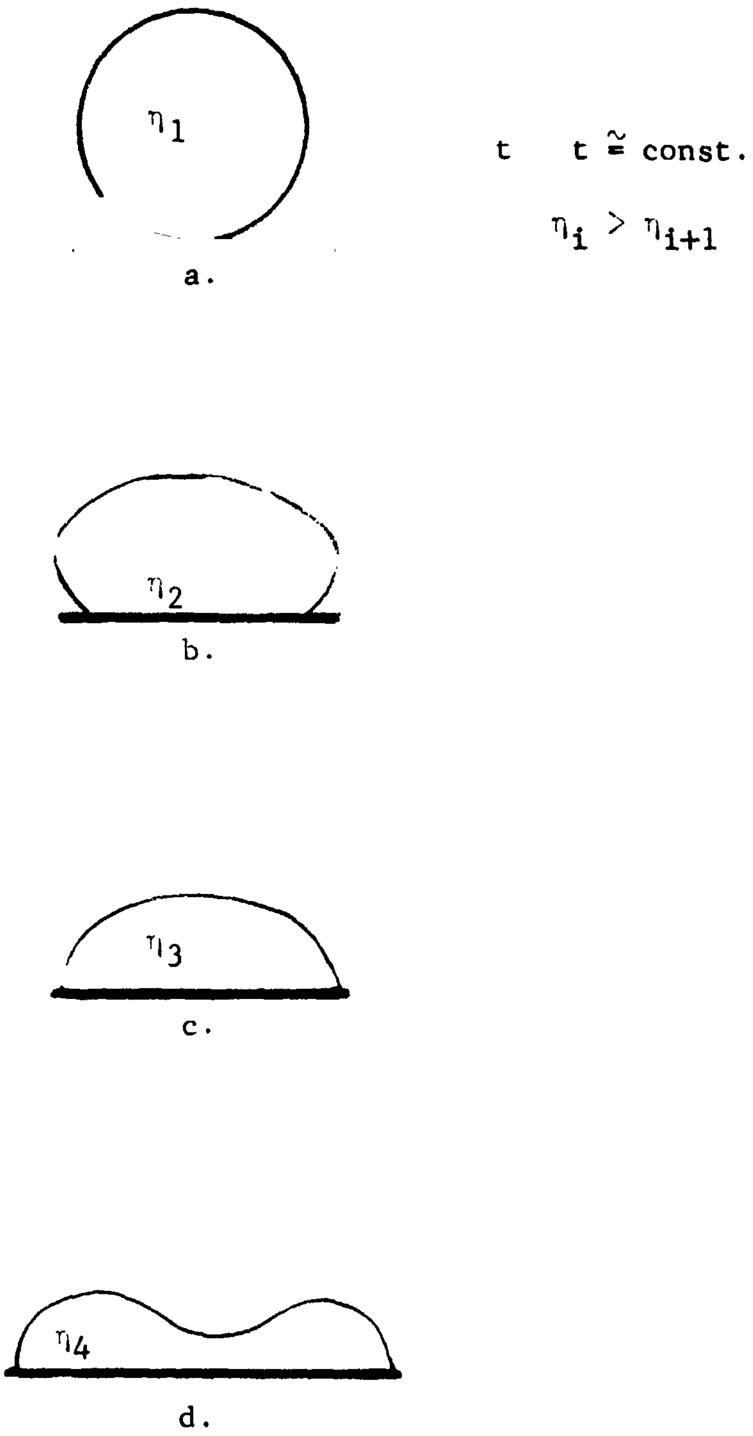

Fig. 19 Droplet Shape as a Function of Decreasing Viscosity

time in the drop tower before contact is made with the chamber walls. Consistent with this increased time, the samples were better able to withstand the wall contact. As the thermal contact with the wall was poorer, due to enhanced sphericity, the samples indicated a slower solid state cooling rate.

Droplet Surface Morphologies

The sphere surface morphologies were varied, but, as noted previously, were not always representative of the internal morphologies. They were also significantly affected by residual solid, contamination, and cooling rate.

Figure 20 illustrates how a particle of residual solid at the sphere surface can act as a solidification nucleus. This results in rapid dendritic growth emanating from the edges of the solid "artifact." These artifacts may be regions stabilized by oxygen or nitrogen contamination or may simply be regions that were not at a temperature greater than the liquidus temperature long enough to completely melt, either during primary melting or during recalescence. They are significantly larger than the critical nuclei needed for solidification and cause a rapid surface solidification. Figure 20a shows this artifact effect using light optics, and Fig. 20b shows the same region with the scanning electron microscope (SEM).

When the cooling was rapid, in addition to having the solidification nuclei present, the surface morphology emanating from these artifact nuclei was an extremely fine dendrite structure with no secondary or tertiary dendrite arms. These are sometimes referred to as Köster predendrites and are shown optically and in the SEM in Fig. 21, respectively. Although these have been reported in chill castings, they are unusual structures for these containerless cooling conditions. It is interesting to note, too,

(a)
Optical
(250X)

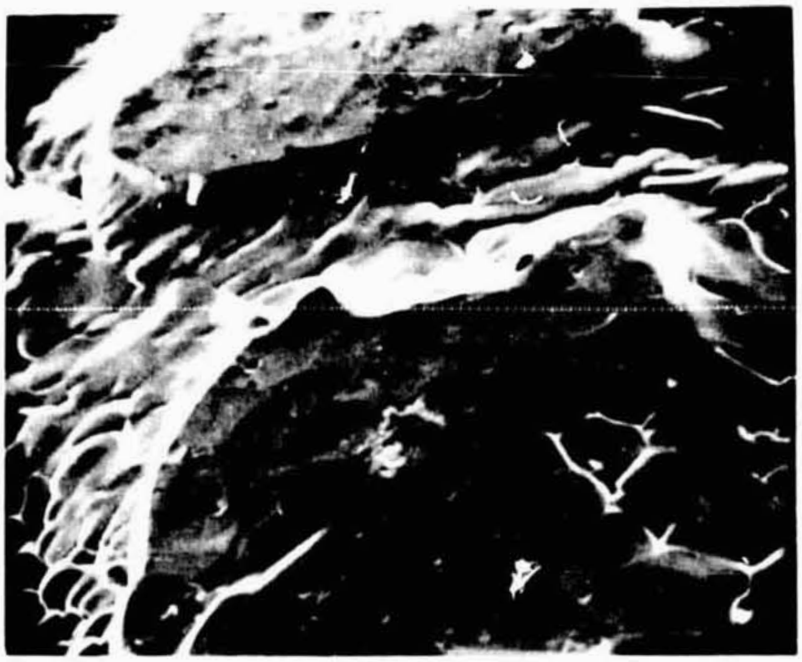

(b)
S.E.M.
(475X)

Fig. 20 Artifact Islands at Sphere Surface
(Surface Morphologies)

Optical
(250X)

S.E.M.
(490X)

Fig. 21 Köster Predendrites on Sphere Surface (Surface Morphologies) that at their furthest extent they seem to demonstrate an effect similar to a vortex. This may be more of an optical effect than actual mapping of the kinematic liquid motion. These microstructures were noted in both the laboratory and drop tower samples.

The surface morphologies of those samples that had the highest degree of sphericity invariably exhibited an equiaxed surface grain morphology. These grains were not always representative of the interior grain structure. That is, they were not always carried through into the interior, and sometimes the interior grain structure could be seen in addition to the equiaxed surface morphology. This is shown in Fig. 22a and is reproduced schematically in Fig. 22b. Although the internal grains are likely to be tied to specific surface grains that were favorably oriented for rapid growth from both the melt and in the solid state, their relationship to these "parent" grains is not always an obvious one. This phenomenon may be concluded to be a surface artifact and a solid state grain growth phenomenon.

Classical dendritic growth was also noted in a limited number of cases, and a particularly good example is shown in Fig. 23. This was for a pure nickel laboratory sample, and the dendrite arms are mutually perpendicular and correspond to ⟨100⟩ directions in the face centered cubic lattice.

An additional surface feature, but one that is not directly related to the solidification process, is shown in Fig. 24. This is at considerably higher magnification and relates only to the 1090 steel samples. This morphological effect is due to the solid state eutectoid transformation in steels. In the case shown, the sample transformed martensitically (without diffusion), and the surface rumpling may be due to this process. Alternatively, the samples may transform by diffusion, forming pearlite rather than

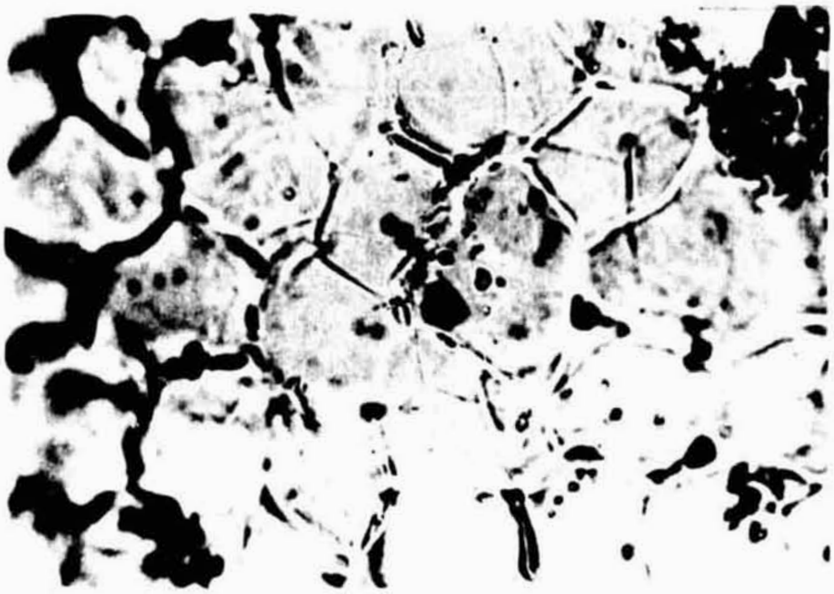

(a)
Optical
(250X)

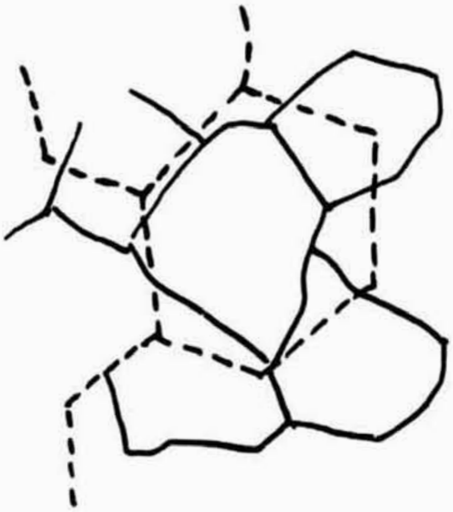

(b)
Schematic

Fig. 22 Equiaxed Surface Grains and Interior Grain Structure (Surface Morphologies)

Optical
(500X)

S.E.M.
(470X)

Fig. 23 Typical Dendritic Growth Structures
(Surface Morphologies)

Metallically
Bright
(Optical)
(1500X)

Fig. 24 Eutectoid Transformation in Steel
(Surface Morphologies)

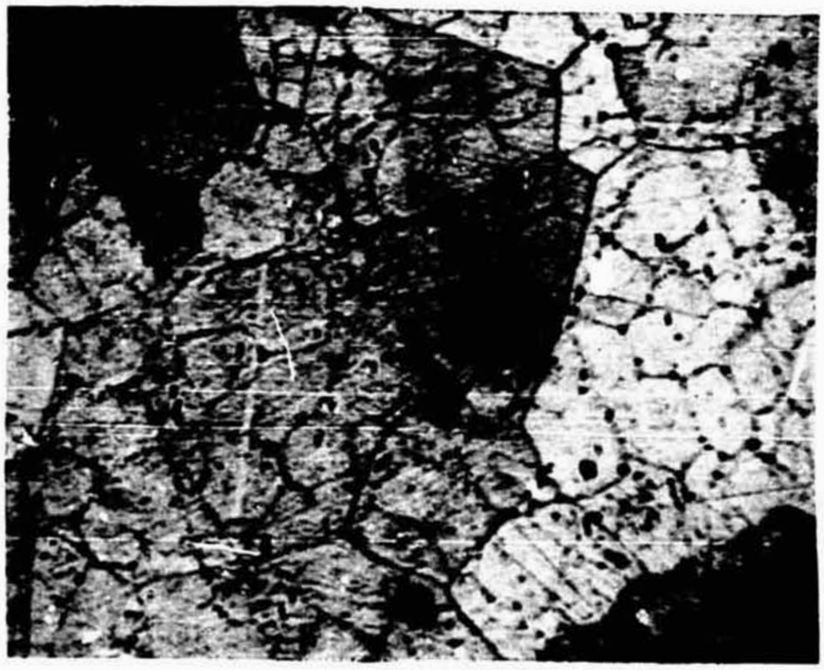

'Ghost'
Grains

Fig. 25 An Example of Surface Ghost Grains
(Internal Morphologies)

martensite, and this also may result in surface rumpling. Martensitic and pearlitic structures were noted in both the laboratory and drop tower samples, but the former was more prevalent in the laboratory samples, implying a faster cooling rate for the laboratory specimens.

One last feature noted is that the samples that lingered for the longest period of time in the free float condition also showed some surface discoloration due to oxidation reactions. This discoloration was most noticeable for the steels, but was noted also for the nickel samples. It is anticipated that improvements in the facility pumping station will correct this situation.

Droplet Internal Morphologies

The majority of the internal morphologies are analogous to those previously mentioned and so this section emphasizes those aspects that are different.

Figure 25 is the reverse of Fig. 22 in that the enlarged internal grains are shown, and, in this near-surface section, the debris from the primary surface structure is superimposed on the equiaxed internal grain structure. This sample is a laborary sample, but this effect was noted for all samples that had moderate or low solid cooling rates.

Figure 26 shows a sample that demonstrates a great deal of internal porosity, as predicted by the solidification theories (Ref. 2). The void area is distributed uniformly throughout the interior of the sphere and may have resulted from rapid solidification due to impact after an external shell had formed.

Figure 27 demonstrates the two primary internal structures noted for the 1090 steel. The varying interior grain morphology is a result of the varying cooling rates on transiting the

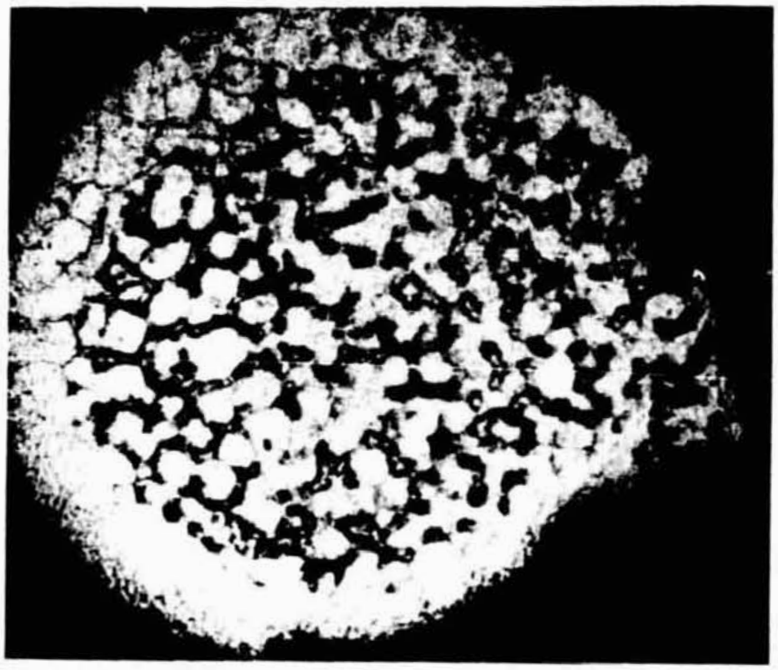

Fig. 26 Internal Voids in Drop Tower Specimen (50X)

eutectoid transformation at 996K, as shown in Fig. 28. This transformation occurs without diffusion (martensitically) on very rapid cooling (Fig. 27a) or with diffusion on slow cooling (Fig. 27b) forming a pearlitic array of alternating lamellae of ferrite and cementite. An intermediate structure is normally anticipated that is referred to as bainite. Figure 29, the isothermal transformation diagram for this steel, would lead us to anticipate this as a prevailing structure for most cooling rates. This, however, was not the case, and the reason is that our experimentation involved continuous cooling. A continuous-cooling transformation diagram is shown in Fig. 30 for a steel that behaves similarly to the 1090 steel utilized in our experimentation. This clearly shows that the readily available I-T diagrams are invalid for continuous cooling, and that the anticipated bainitic transformation is virtually

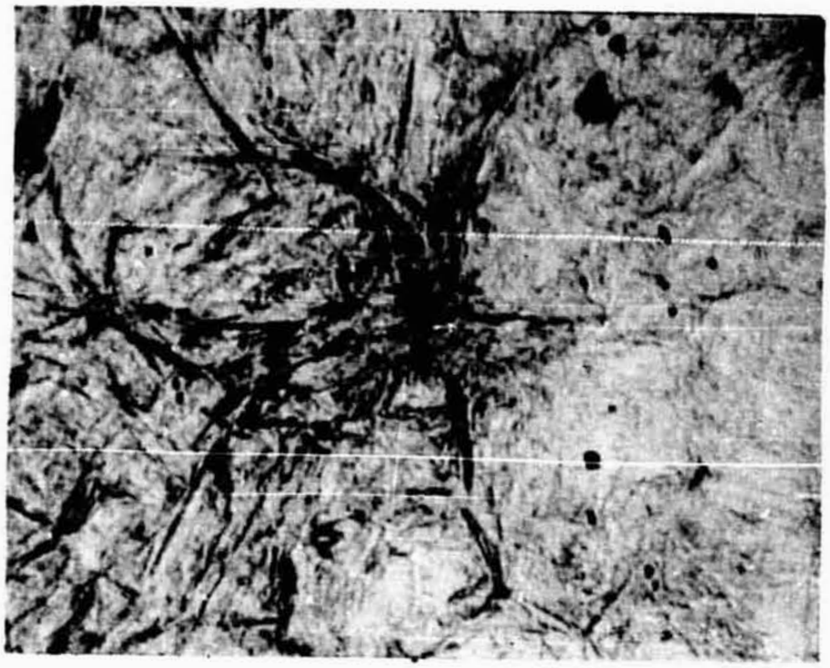

(a)
Martensitic
(1500X)

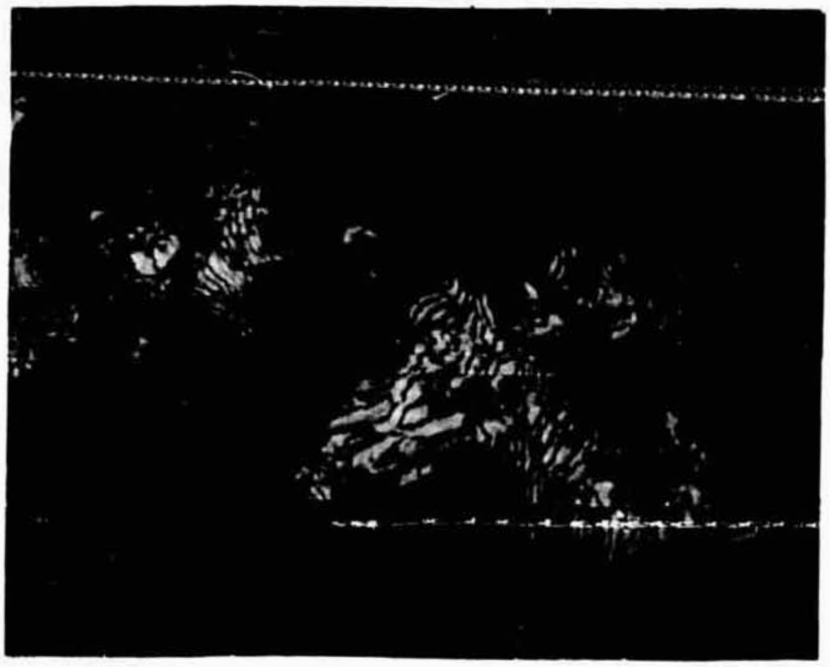

(b)
Pearlitic
(1500X)

Fig. 27 Two Primary Internal Structures for Steel Specimens (Internal Morphologies)

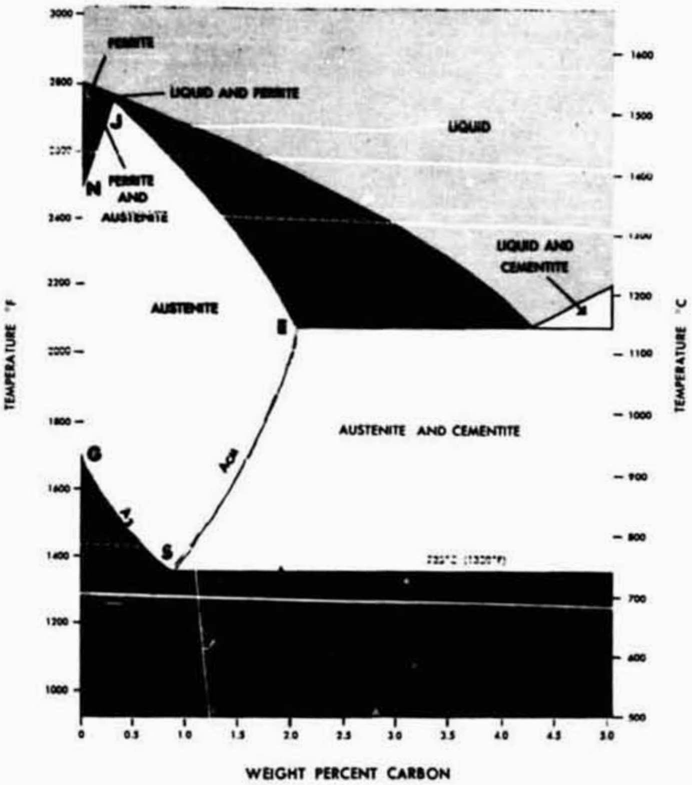

Fig. 28 Iron-Iron Carbide Phase Diagram

completely shrouded by the martensitic and pearlitic reactions. As a result, no appreciable bainite is formed nor should be anticipated.

One final effect should be noted for the steel samples: Although this is a surface effect, it is most clearly demonstrated by showing the near-surface microstructure (Fig. 31). Clearly, there has been an appreciable loss in carbon, and reference to Fig. 28 will show that carbon loss will result in increased amounts of proeutectoid ferrite (white) and reduced amounts of pearlite. This is exactly what is shown in Fig. 31.

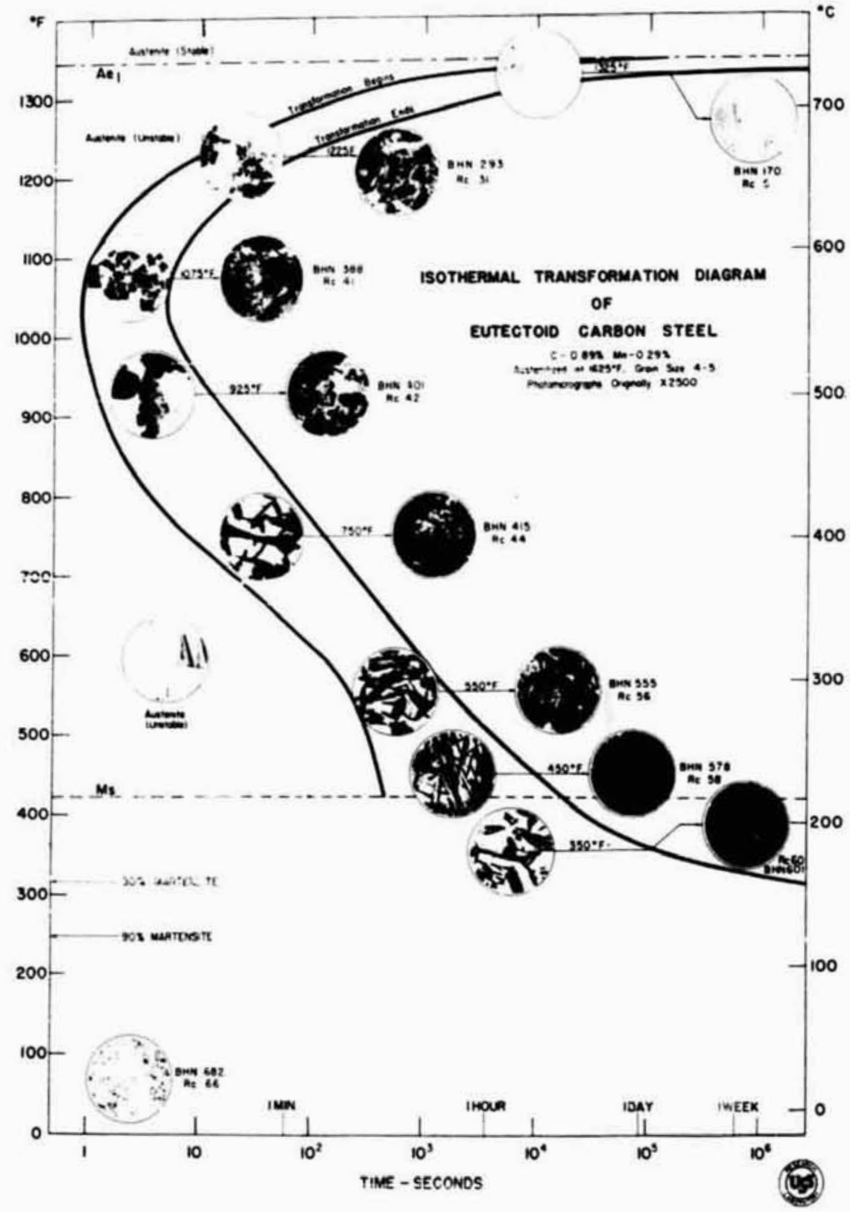

Pearlite

Bainite

Martensite

Fig. 29 Isothermal Transformation Diagram for Steel

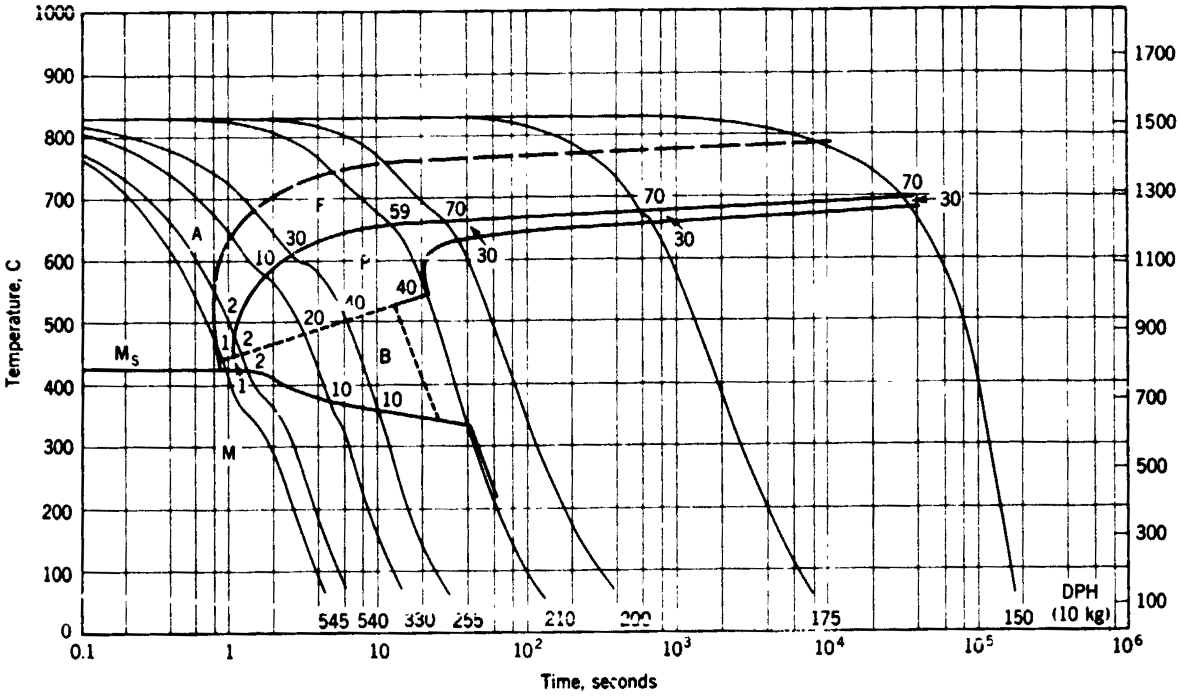

Fig. 30 Continuous Cooling Diagram for Steel

Decarburized
Region
(1500X)

Fig. 31 Carbon Depletion in Steel Droplet
(Internal Morphologies)

In conclusion, we may say that the macroscopic and microscopic morphologies vary appreciably, but consideration or extension of the available technology base is capable of explaining the variations.

CONCLUSIONS AND RECOMMENDATIONS

Direct resistance melting of wire specimens has proven to be a very effective way of preparing molten metal specimens in any limited time zero gravity facility. In the first series of drops, we successfully melted and resolidified both nickel and steel specimens during the three seconds of free fall.

Because of a lack of control over cooling rate, droplets with true spherical symmetry in the grains were not realized. Droplets were cooling from the outside in toward the center and there were strong indications on some specimens of material depletion at the center of the droplet.

Shadow grains were in evidence on several specimens. An equiaxed surface grain often had a well ordered hexagonal grain just below it, which was visible in the surface micrographs. This is a solid state, grain growth phenomenon.

Many of the specimens contacted the container wall before solidification was complete. The phenomena of very rapid cooling after a pattern of grain structure had been established introduce structures that are quite different from that found on droplets that completely solidified before contacting the container wall. The partially solidified specimens are experiencing essentially a rapid quench at a point in the cooling cycle. Structures formed under these conditions need more analytical and empirical study.

A film technique for measuring temperature of the free floating droplet was developed during the contract. Although refinements are needed, temperature-time histories of the droplets were computed.

From the first two series of drops, several needed modifications to the apparatus became evident. Specimen size scale-up proved more difficult than anticipated. It appears now that only through added control in the specimen heating circuit can we hope to reach the size limit dictated by cooling time available.

The melting process has introduced more forces on the specimen than was originally anticipated. The forces seem to be primarily due to an elongation in the wire specimen just prior to unduloid formation. Since we have no way of controlling specimen motion after the droplets formed, it becomes very important that the droplets are released with little or no accelerating forces. Careful study of the wire melting process in the laboratory should lead to ways of minimizing these forces.

With an improved apparatus, the next series of drops in the MSFC drop tower will allow another step forward in the understanding of metals solidifying in a zero gravity environment.

REFERENCES

1. McAnelly, W. B. and Covington, S. S., Low-Gravity Fluid Mechanics Drop Tower Facility, NASA Tech. Memorandum No. 53817, February 1969.
2. Li, C. H., "Segregation Effects during Solidification in Weightless Melts," Grumman Research Proposal RP-425, July 1971.
3. Li, C. H., "Segregation Effects during Solidification in Weightless Melts," Final Report on NASA Contract NAS 8-27891, June 1973.
4. Kattamis, T. Z. and Flemings, M. C., Prod. Casting, Vol. 52, No. 1, 1967, p. 191.
5. Kattamis, T. Z., Current Investigations, Department of Metallurgy, Institute of Materials Science, University of Connecticut, Stans, Connecticut.
6. Chace, W. G., Liquid Behavior of Exploding Wires," Physics of Fluids, Vol. 2, No. 2, March-April 1959.
7. Paynter, H. L., AIAA Jour., Vol. 2, p. 1624, 1964.
8. Reichman, J., "Solidification of Molten Spheres in Vacuum," Grumman Research Department Memorandum, RM-544, June 1972.
9. Service Manual for Apparatus to Be Used in NASA/MSFC Drop Tower in Investigating Metal Solidification in Zero Gravity (Contract NAS 8-28604), December 1972.
10. Busch, G. and Hilgeman, T., "A Photographic Technique for Measuring Temperatures," Grumman Research Department Memorandum, to be published.
11. Zisman, W., "Spreading of Oils on Water," J. Chem. Phys., Vol. 9, p. 534, July 1941.

APPENDIX

CALCULATION OF TEMPERATURE AND ENERGY FROM VOLTAGE AND CURRENT MEASUREMENTS

During each drop, voltage and current in the specimen circuit were telemetered to a central receiving station. This information was used to compute a time history of energy and a final specimen temperature. The analysis for each of these calculations is presented in this Appendix.

Energy Computation

Current and voltage were read from the telemetry records at every 0.010 second. The data for Run T3 are given in Table A-1. The product was then plotted to give a power time history. A typical power curve (taken from data of Run T3) is shown in Fig. A-1.

TABLE A-1 RUN NO. T3 (0.051 cm dia Ni)

Time	Current	Voltage	Calculated Wattage	Calculated Resistance
0	406	25.24	10,247	62.167
0.01	218	26.19	5,709	120.138
0.02	156	27.62	4,309	177.051
0.025	125	28.57	3,571	228.560
(Wire Separation)				

The power curve was numerically integrated to obtain the energy as a function of time. The energy curve from the integrated power curve is shown in Fig. A-2. Energy curves for all of the first series of runs were computed in this manner and are presented in the main text.

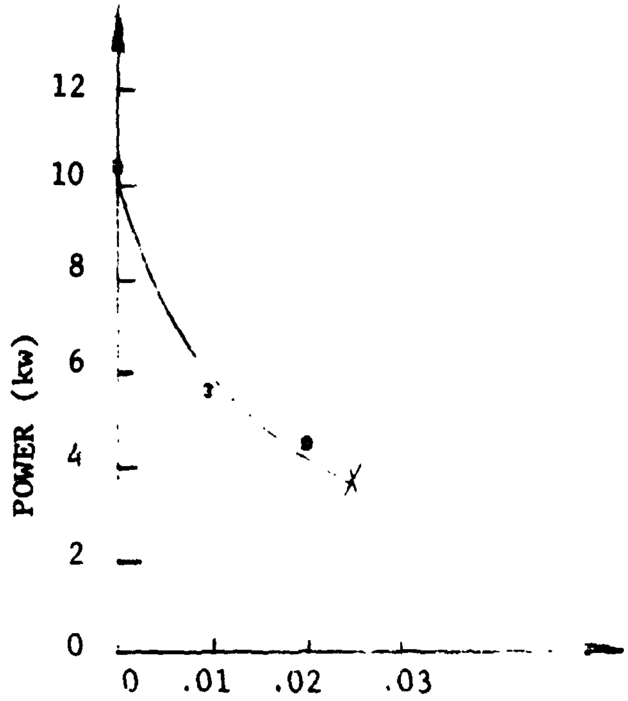

TIME (sec)

Fig. A-1 Time History of Power for Run T3

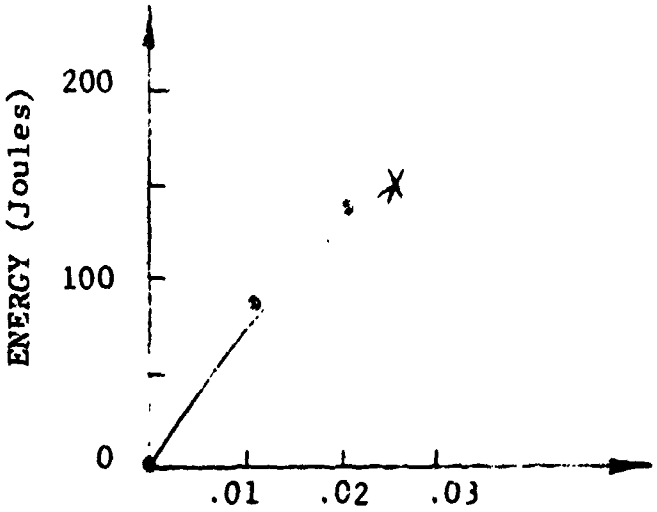

TIME (sec)

Fig. A-2 Time History of Energy for Run T3

Temperature Calculations

To obtain the final nickel specimen temperature, a linear relation between temperature and resistance was assumed. Thus the resistance at any temperature, T, is related to the resistance at $0°C$ by

$$R_T = R_o(1 + \alpha T) \ .$$

The temperature coefficient of resistance, α, is the proportionality constant and is given in the literature (Ref. A-1) for most materials. A value of 0.0047 per °C was used in this report. For $T = 20°C$ this becomes

$$R_{20} = R_o \ (1 + 20\alpha)$$

The ratio of R_T/R_{20} is then equal

$$\frac{R_T}{R_{20}} = \frac{1 + \alpha T}{1 + 20\alpha} = \frac{1}{1 + 20\alpha} + \frac{\alpha}{1 + 20\alpha} T$$

For the value of $\alpha = 0.0047$,

$$\frac{R_T}{R_{20}} = 0.914 + 0.0043T$$

This equation is plotted in Fig. A-3.

For steel the relationship was nonlinear and taken from Ref. A-1. The curve for steel is also plotted on Fig. A-3.

The resistance was plotted as a function of time by computing E/I at 0.01 second intervals from the telemetry charts. A typical resistance curve is shown in Fig. A-4. These data were taken from Run T3 also. To compute the final specimen temperature, the final resistance was read from the time history and

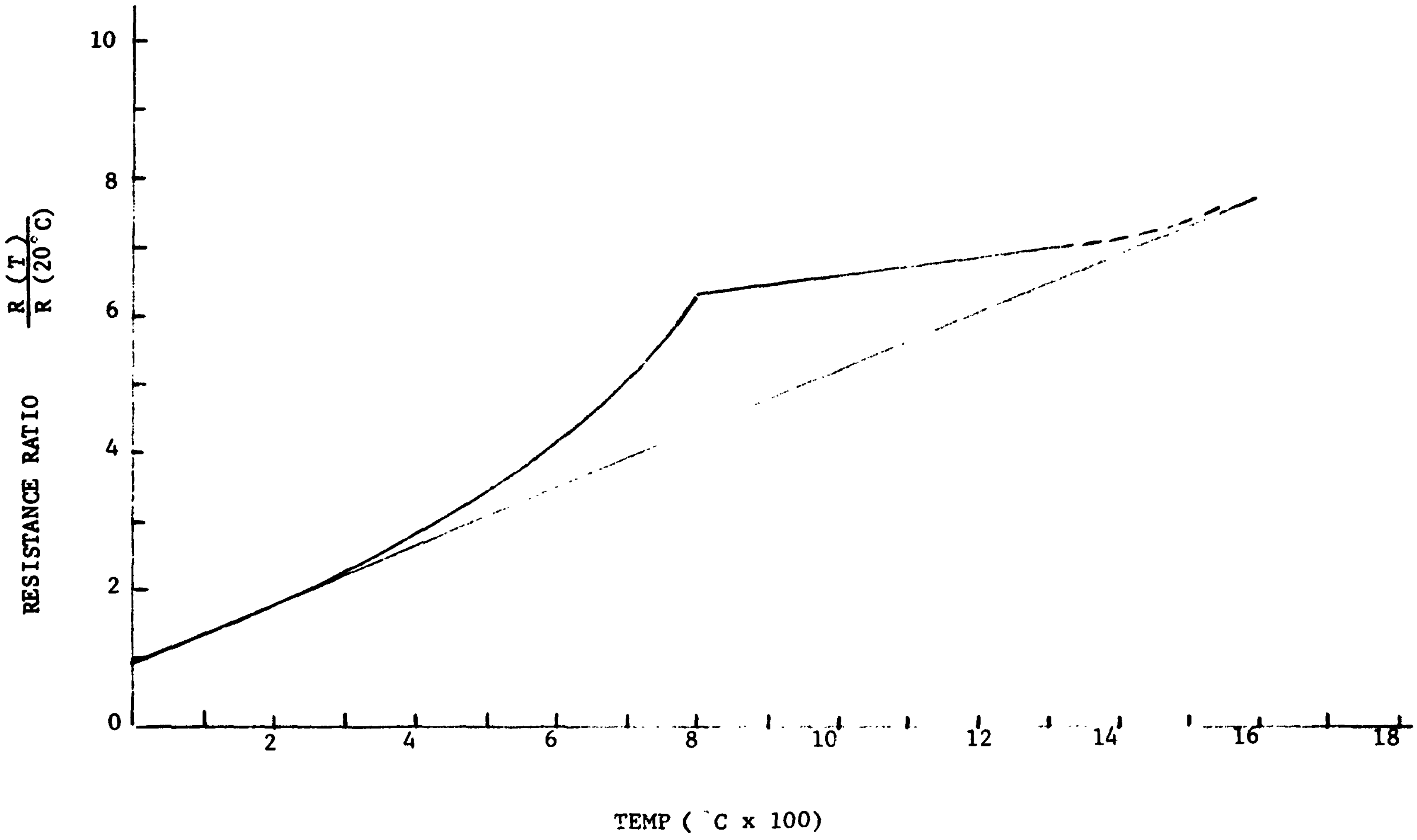

Fig. A-3 Resistance Ratio versus Temperature for Steel and Nickel

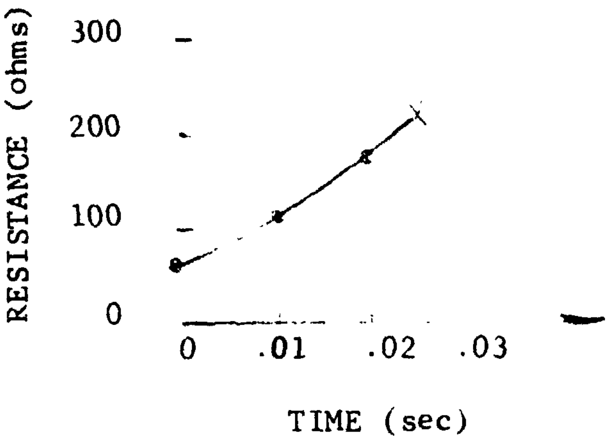

Fig. A-4 Time History of Resistance for Run T3

divided by the resistance at 20°C. The ratio was used with the curves in Fig. A-3 to read final temperature.

The resistance at 20°C was computed from the resistivity ρ. The resistivity was taken from the literature (Ref. A-1). The values used were

Nickel	9.5μΩ-cm (0°C)
Steel	18.0μΩ-cm (20°C)

The resistance for nickel at 20°C is then equal to

$$R_{20} = R_o (1 + \alpha T_{20})$$

$$= \rho_o \frac{\ell}{A} (1 + \alpha T_{20})$$

where ℓ is the length of the specimen and A is the cross-sectional area.

The resistance for steel at 20°C is then equal to

$$R_{20} = \rho_{20} \frac{\ell}{A}$$

Since the variation of the characteristic constants of any material depend upon physical changes in the material, the relationships are often quite complex and certainly not linear. For the calculations in this Appendix, this is true for the temperature coefficient of resistance. Over small temperature ranges, the linear relationship is quite accurate. But, from room temperature to melt temperature where the material is undergoing several complex physical and chemical changes, this assumption probably introduces appreciable error. This explains why a material like pure nickel is more amenable to the calculations than a complex alloy like 1090 steel.

Reference

A-1 Lyman, T., Metals Handbook of the ASM, The American Society for Metals, 1948.